

Department of Physics and Astronomy

University of Heidelberg

Diploma thesis
in Physics

submitted by

Peter Klaus Martin Weidenkaff

born in Heidelberg, Germany

Februar 2010

Study of $D^0 - \bar{D}^0$ mixing with the LHCb detector

*This diploma thesis has been carried out by Peter Klaus Martin Weidenkaff at
the
Physical Institute
under the supervision of
Prof. Dr. Ulrich Uwer*

Abstract

This work presents a simulation study to measure $D^0 - \bar{D}^0$ mixing with the LHCb detector. Tagged wrong sign $D^0 \rightarrow K^+\pi^-$ and right sign $D^0 \rightarrow K^-\pi^+$ decays are used. The D^0 's are required to originate from $D^* \rightarrow D^0\pi$ decays in order to tag the production flavour of the D^0 . The selection of the signal is presented and the various types of backgrounds are discussed. The expected ratio of signal to background is estimated to be $S/B \approx 0.19$. Signal candidates are filtered by the Level 0 hardware trigger and the first stage of the high level software trigger with an efficiency of $(31.1 \pm 1.1)\%$. The expected signal yield for an integrated luminosity of 100pb^{-1} is 1.8×10^6 selected and triggered right sign events. It was found that the effective D^0 lifetime resolution is approximately 47 ps for D^0 's from D^* 's which are directly produced in the proton-proton collision. Furthermore the effect of a D^0 lifetime dependent acceptance due to trigger and selection on the mixing parameters is studied.

Kurzfassung

In dieser Arbeit wird eine Simulationsstudie zur Messung der $D^0 - \bar{D}^0$ Mischung mit dem LHCb detector vorgestellt. Es werden „wrong sign“ $D^0 \rightarrow K^+\pi^-$ und „right sign“ $D^0 \rightarrow K^-\pi^+$ Zerfälle untersucht, wobei das D^0 Meson aus dem Zerfall $D^* \rightarrow D^0\pi$ stammt. Dadurch kann der Quarkinhalt des D^0 zum Produktionszeitpunkt bestimmt werden. Die Selektion der Signalzerfälle wird gezeigt und die verschiedenen Untergründe werden diskutiert. Das Verhältnis von Signal zu Untergrund wird auf $S/B \approx 0.19$ geschätzt. Die Signalzerfälle werden vom Level 0 Hardwaretrigger und der ersten Instanz des Softwaretriggers mit einer Effizienz von $(31.1 \pm 1.1)\%$ gefiltert. Bei einer integrierten Luminosität von 100pb^{-1} werden 1.8×10^6 „right sign“ Zerfälle erwartet. Die effektive Lebenszeitauflösung der D^0 Kandidaten aus D^* 's, welche wiederum direkt in einer Proton-Proton Kollision erzeugt wurden, beträgt ungefähr 47ps. Desweiteren wird die, von der D^0 Lebenszeit abhängige, Akzeptanz der Selektion und des Triggers und deren Auswirkung auf die Mischungsparameter untersucht.

Contents

1	Introduction	9
2	Phenomenology of charm mixing	11
3	The LHCb experiment	15
3.1	Tracking system	16
3.1.1	Vertex locator	18
3.1.2	Trigger Tracker	19
3.1.3	Main tracker	19
3.2	Calorimeter system	21
3.3	Muon system	22
3.4	Particle identification system	23
3.5	Trigger system	23
3.5.1	L0 hardware trigger	24
3.5.2	First stage of the high level software trigger	24
3.5.3	Second stage of the high level software trigger	25
4	Measurement principle and experimental status	27
4.1	Measurement principle	27
4.2	Experimental status	30
5	Monte Carlo simulation	33
5.1	Signal sample	33
5.2	Minimum bias sample	34
6	Selection	35
6.1	Kinematic selection quantities	37
6.1.1	Momentum	37

6.1.2	Impact parameter	39
6.1.3	Flight distance significance	39
6.1.4	Pointing variables	41
6.2	Particle identification	42
6.3	Track and vertex quality	44
6.4	Selection results	48
6.5	D^0 lifetime dependence on selection	48
7	Background	51
7.1	Secondary D^* background	52
7.2	Combinatoric random π_S background	53
7.3	Partially reconstructed B background	56
7.4	Combinatoric D^0 background	56
7.5	Low mass background	58
7.6	Reflection background	58
8	Trigger	61
8.1	Trigger efficiencies and trigger lines	61
8.2	D^0 lifetime dependent acceptance	63
9	D^0 lifetime and lifetime resolution	65
9.1	Vertex and D^0 lifetime resolution	66
9.2	D^0 lifetime acceptance	67
10	Signal yield	71
10.1	Signal probability density function	73
10.2	Background probability density functions	73
10.3	Fit results	74
10.4	Alternative method of the signal yield determination	76
10.5	Expected signal yield	77
11	Extraction of the mixing parameters	79
11.1	Influence of D^0 lifetime acceptance	81
11.2	Influence of background contribution	84
12	Summary and Conclusion	87

Chapter 1

Introduction

The Large Hadron Collider (LHC) at CERN in Geneva is the world's highest-energy particle accelerator. First collisions were observed in November 2009. The large center of mass energy will allow to explore physics beyond the well tested electroweak scale (~ 90 GeV). In particular, the experiments at the LHC will answer the question of the electroweak symmetry breaking which, in the Standard Model, is explained through the Higgs mechanism and the Higgs mechanism predicts a heavy scalar Higgs Boson. The search for physics beyond predictions of the Standard Model is a second goal of the LHC.

The LHC-beauty experiment (LHCb) is one of six detector experiments at the LHC and it is dedicated to the precision measurements of rare B meson decays. It is designed as single arm spectrometer covering the very forward region of $2 < \eta^1 < 5$. The detector provides an excellent vertex and momentum resolution and a good particle identification. With these qualities it is also a promising detector to study charm meson decays. One of the interesting physics topics of charm mesons is the precise measurement of charm mixing and the study of possible \mathcal{CP} violation.

D^0 - \bar{D}^0 oscillation is now, after evidences from BaBar [1] and CDF [2], a well-established phenomena. Contrary to the B meson and kaon system the D^0 mixing involves down type quarks in the quantum loop corrections. The precise measurement of D^0 mixing therefore offers an excellent tools to search for possible contributions of new physics effects to the down type quark sector. During one year of LHC operation 10^{13} $c\bar{c}$ events will be produced in the acceptance of LHCb.

¹The pseudo rapidity η is defines as $\eta = -\ln\{\tan(\frac{\theta}{2})\}$. The angle θ is the angle between particle momentum and beam axis.

With this large data sample it is expected that LHCb will significantly improve the accuracy of the measurement of the mixing parameters. In this work a simulation study to measure $D^0 - \bar{D}^0$ mixing using $D^0 \rightarrow K\pi$ decays with LHCb is presented.

In the next chapter an overview about the phenomenology of $D^0 - \bar{D}^0$ mixing is given and in Chapter 3 the LHCb experiment is described. The analysis strategy and the experimental status is presented in Chapter 4, the selection of the signal is shown in Chapter 6. Chapter 7 covers the results of background studies and Chapter 8 discusses trigger issues concerning the analysis. The D^0 lifetime resolution and the lifetime dependent acceptance are studied in Chapter 9 and the determination of the signal yield is shown in Chapter 10. Finally, in Chapter 11 the results of a Monte Carlo study to estimate the expected sensitivity is presented.

Chapter 2

Phenomenology of charm mixing

In this section, a short overview about the phenomenology of $D^0 - \bar{D}^0$ mixing is given. A detailed description can be found in [3].

D^0 mesons are created in strong processes as well defined flavour states. These states are neither eigenstates of the weak interaction nor mass eigenstates. As a consequence, a particle created as D^0 at $t=0$ evolves in time into a mixture of D^0 and \bar{D}^0 . Phenomenological, the time development of the D^0 meson can be described by a 2-dim Schrödinger equation using a 2-dim effective Hamiltonian:

$$\mathcal{H}_{eff} = \mathbf{M} - \frac{i}{2}\mathbf{\Gamma} \quad (2.1)$$

$$i\frac{\partial}{\partial t} \begin{pmatrix} D^0(t) \\ \bar{D}^0(t) \end{pmatrix} = \mathcal{H}_{eff} \begin{pmatrix} D^0(t) \\ \bar{D}^0(t) \end{pmatrix} \quad (2.2)$$

The matrices \mathbf{M} and $\mathbf{\Gamma}$ are 2x2 Hermitian matrices with $M_{ij} = M_{ji}^*$ and $\Gamma_{ij} = \Gamma_{ji}^*$. CPT invariance requires for the diagonal elements $M_{11} = M_{22}$ and $\Gamma_{11} = \Gamma_{22}$. For the case of \mathcal{CP} conservation one finds $M_{12} = M_{21}$ and $\Gamma_{12} = \Gamma_{12}$. Diagonalization leads to mass eigenstates $|D_1\rangle$ and $|D_2\rangle$ that are linear combinations of the flavour eigenstates $|D^0\rangle$ and $|\bar{D}^0\rangle$:

$$|D_{1,2}\rangle = p|D^0\rangle \pm q|\bar{D}^0\rangle. \quad (2.3)$$

The complex parameters q and p obey the normalization condition $|q|^2 + |p|^2 = 1$. We define the eigenvalues of the Hamilton operator: $\lambda_{1,2} = M_{1,2} \pm i\Gamma_{1,2}/2$. The difference of the eigenvalues squared is $\Delta\lambda^2 = 4(M_{12} + i\Gamma_{12}/2) * (M_{12}^* + i\Gamma_{12}^*/2)$.

$M_{1,2}$ and $\Gamma_{1,2}$ are the mass and decay width of the two mass states. Using one of the eigenfunction equations of the Hamilton operator we can calculate the ratio of the complex factors q and p :

$$\frac{q}{p} = \pm \frac{\sqrt{M_{12}^* + i\Gamma_{12}^*/2}}{\sqrt{M_{12} + i\Gamma_{12}/2}} = \left| \frac{q}{p} \right| e^{-i\phi} \quad (2.4)$$

The time evolution of the mass eigenstates is defined by the Schrödinger equation:

$$|D_{1,2}(t)\rangle = \exp^{-i\lambda_{1,2}t} |D_{1,2}(0)\rangle \quad (2.5)$$

For a $|D^0\rangle$ produced at $t=0$ the probability to find the state $|D^0\rangle$ after a certain time t is given by [4]:

$$I(D^0 \rightarrow D^0; t) := |\langle D^0 | D^0(t) \rangle|^2 = \frac{e^{-\Gamma t}}{2} \{ \cosh(y\Gamma t) + \cos(x\Gamma t) \} \quad (2.6)$$

and the probability to find instead the state $|\bar{D}^0\rangle$ is:

$$I(D^0 \rightarrow \bar{D}^0; t) := |\langle \bar{D}^0 | D^0(t) \rangle|^2 = \frac{e^{-\Gamma t}}{2} \left| \frac{p}{q} \right|^2 \{ \cosh(y\Gamma t) - \cos(x\Gamma t) \} \quad (2.7)$$

With $\Gamma := (\Gamma_1 + \Gamma_2)/2$ and the mixing parameters:

$$x = \frac{2(M_1 - M_2)}{\Gamma_1 + \Gamma_2} \quad y = \frac{\Gamma_1 - \Gamma_2}{\Gamma_1 + \Gamma_2} \quad (2.8)$$

Mixing will occur if either x or y are non-zero. Depending on the size of the mixing parameters an oscillating behavior can be observed, like in the B_s system.

In addition, there might be \mathcal{CP} violation. \mathcal{CP} violation can be parametrized using the quantity λ_f [5]:

$$\lambda_f := \frac{q}{p} \frac{A_f}{\bar{A}_f} = \left| \frac{q}{p} \right| r_d e^{-i(-\delta_f + \phi)} \quad (2.9)$$

Here, $-\delta_f$ is the relative phase between the decay amplitudes $A_f = \langle f | \mathcal{H} | D^0 \rangle$ and $\bar{A}_f = \langle f | \mathcal{H} | \bar{D}^0 \rangle$ of a D^0 or \bar{D}^0 decaying to a final state f and r_d is the magnitude of the ratio between the two amplitudes. \mathcal{CP} symmetry can be violated in three ways:

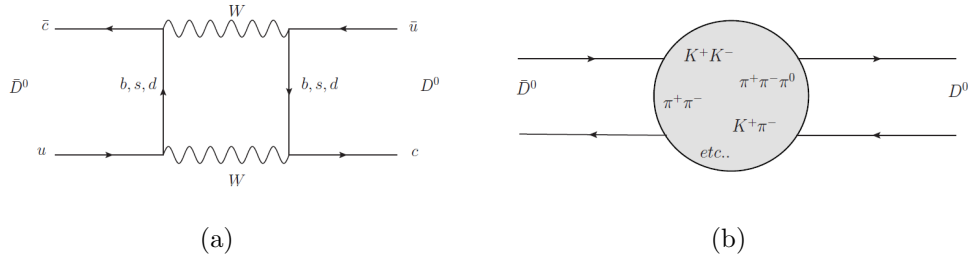


Figure 2.1: Mixing in Standard Model: (a) short range contributions ('box diagrams') and (b) long range contributions with intermediate hadronhadron states. Figure taken from [5].

- A value for $A_f/\bar{A}_f \neq 1$ would indicate \mathcal{CP} violation in the decay. This means that the decay amplitude for D^0 to a final state f is different from the decay amplitude of \bar{D}^0 to the same final state.
- In the case of $|q/p| \neq 1$ \mathcal{CP} symmetry is violated in mixing. This implies that the mixing probability for a D^0 is different from a \bar{D}^0 .
- When $A_f/\bar{A}_f \neq 1$ as well as $|q/p| \neq 1$, this denotes that $\phi \neq 0$, \mathcal{CP} symmetry is violated in the interference of decay and mixing.

Charm mixing has contributions from 'short range' physics processes, so called 'box-diagrams' (Figure 2.1(a)), and from long-range processes with intermediate hadron states (Figure 2.1(b)). In contrast to mixing in the B meson and kaon system, charm mixing involves down type quarks in the 'box-diagrams'. In the Standard Model(SM) short distance contributions are small because the exchange of b-quarks is CKM suppressed and d+s-quarks are suppressed due to the GIM cancellation mechanism. Values of lowest order calculations of the short range contribution are $x_{box} \approx \mathcal{O}(10^{-5})$ and $y_{box} \approx \mathcal{O}(10^{-7})$ [6]. Calculations of higher orders in the operator product expansion yields values for x and y of $\mathcal{O}(10^{-3})$ [7]. Furthermore, it is difficult to calculate the long-range contribution in the SM. Precise measurements of the mixing parameters can help to improve the accuracy of the calculations.

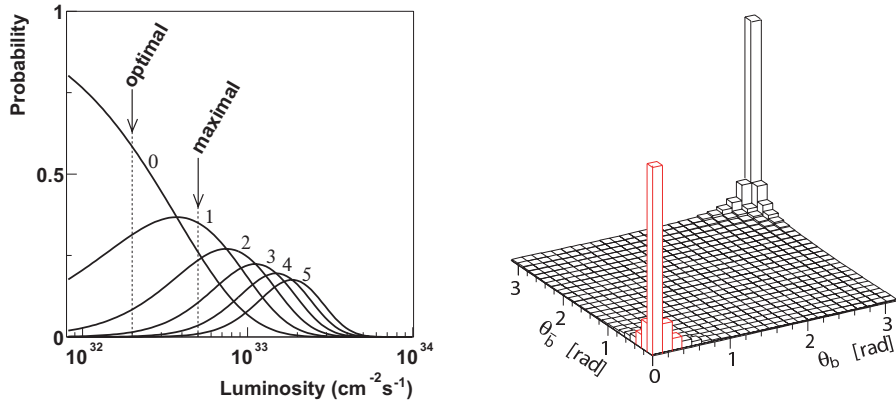
In the Standard Model \mathcal{CP} violation is expected to be below the sensitivity of the experiments and therefore the detection of \mathcal{CP} violation in charm mixing, either in the interference between decay and mixing or in the mixing itself, would be a unambiguous sign for new physics [8].

Chapter 3

The LHCb experiment

The LHCb detector is located at the Large Hadron Collider (LHC) at CERN in Geneva. The LHC is designed to provide a center of mass energy of 14 TeV and after a short pilot run in 2008 first collisions were seen in November 2009. At nominal conditions the LHC has a bunch crossing rate of 40 MHz. The number of single and multiple proton-proton interactions depends on the instantaneous luminosity and is shown in Figure 3.1(a). An instantaneous luminosity between $2 \cdot 10^{32} \text{cm}^{-2} \text{s}^{-1}$ (optimal) and $5 \cdot 10^{32} \text{cm}^{-2} \text{s}^{-1}$ (maximal) will be provided. For nominal luminosity 0.7 interactions per bunch crossing and a rate of visible interactions, i.e. interactions which leave at least five tracks in the detector, of 14 MHz are expected. The integrated luminosity of one year (10^7s) of running at nominal conditions is 2fb^{-1} .

LHCb is a dedicated experiment for B meson physics. Especially it is designed for precise measurements of \mathcal{CP} violation and rare B decays. LHCb is built as a single-arm forward spectrometer because most likely $b\bar{b}$ pairs produced in a proton-proton interaction fly into the same direction. The correlation between the polar angles of the b and the \bar{b} quark is shown in Figure 3.1(b). Therefore 25% of all produced B mesons produced lie in the detector acceptance. The LHCb detector covers an acceptance between 10 and 300 mrad in the bending plane (x-axis) of the magnet and between 10-250 mrad in the non-bending plane (y-axis). The Layout of the detector is presented in Figure 3.2. In the following the detector is described in detail. The different parts can be categorized as tracking system, calorimeter system, the muon stations and particle identification system. In the last section the LHCb trigger system is introduced.



(a) Number of interactions as a function of instantaneous luminosity. (b) correlation between polar angles of b and \bar{b} .

Figure 3.1: (a) Mean number of interactions as a function of the instantaneous luminosity. (b) Simulated correlation of the polar angles of the $b\bar{b}$ pair. Figures from [9]

3.1 Tracking system

The tracking system consists of the vertex locator (VELO), the trigger tracker (TT) and the main tracker (T-Stations). The dipole magnet [11] is located between TT and T-Stations and has an integrated magnetic field of:

$$\int B dl = 4.2 Tm \quad (3.1)$$

Charged particles traversing the detector are bended by the dipole magnet and the bending radius can be measured using the vertex Locator (VELO) before the magnet and the T-Stations after the magnet. The tracking stations are placed in essentially field free regions and thus it can be assumed that in first order the particle tracks are straight in the VELO and T-Stations. The bending of the tracks in the magnet can be approximated by a 'momentum kick' in the center of the magnet, and the reconstructed tracks from VELO and T-Stations can be extrapolated as straight lines to the center of the magnet. The momentum of a particle is proportional to the difference of the track slopes in VELO and T-Stations. Nevertheless especially in the T-Stations there is a considerable fringe field and thus corrections need to be applied to this momentum kick method.

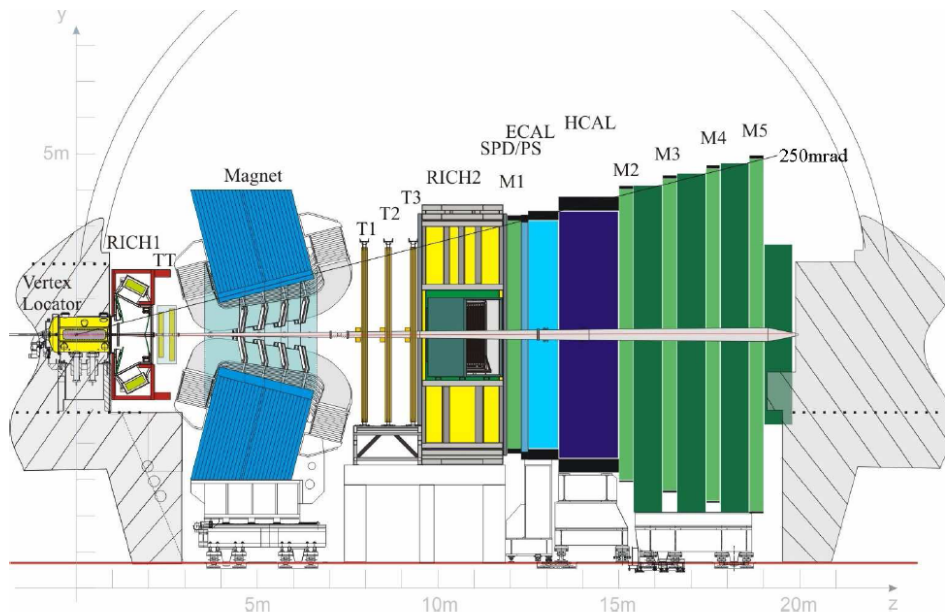


Figure 3.2: Layout of the LHCb detector. The horizontal axis is along the beam pipe (z -axis) and the vertical axis is in the non-bending plane of the magnet (y -axis). Shown are (from left to right) the vertex locator (VELO), the first RICH detector (RICH1), the trigger tracker (TT), the dipole magnet, the main tracker (T-Stations), the second RICH detector (RICH2), the Scintillating Pad Detector (SPD), the Preshower detector (PS), the electromagnetic (ECAL) and hadronic (HCAL) calorimeters and on the right side the five muon stations. From [10].

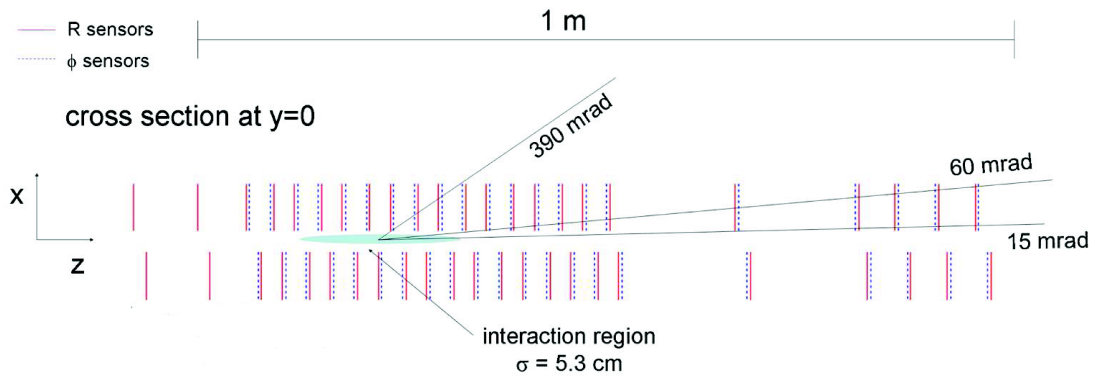


Figure 3.3: Cross section at $y=0$ of the vertex locator(VELO). The 21 stations with R and ϕ sensors are shown. The VELO is closely located around the interaction region.

LHCb will have a relative momentum resolution between 0.35% and 0.55% (dependent on the track momentum) for tracks that are reconstructed in VELO and T-Stations [10].

3.1.1 Vertex locator

The vertex locator (VELO) [12] is positioned closely around the interaction point. It consists of 21 stations each with two different sensor types. The so-called R-sensors measure the radial distance from the beam and the ϕ -sensors are able to determine the angular position of a track. A track can be measured up to a minimal distance of 8mm from the beam pipe and the extrapolation to the interaction point and therefore it is very accurate. The geometry of the VELO is sketched in a x-z projection in Figure 3.3. Due to the fact that there is no beam pipe around the interaction point the VELO itself needs to be in a vacuum. The high vacuum of the LHC is separated by a thin aluminum foil from the VELO vacuum. Instable beam conditions can destroy the VELO and therefore the VELO can be moved away from the beam pipe during beam injection.

3.1.2 Trigger Tracker

The Trigger Tracker (TT) [10] is placed in front of the magnet and consists of two stations. Every station has two layers of silicon strip detectors. The second layer of the first station and the first layer of the second station are rotated by $\pm 5^\circ$ in order to provide a resolution in y -direction. The other layers are arranged parallel to the y -axis. The dipole magnet can bend low energetic particles out of the acceptance of the main tracker and in this case the TT is used to measure the momentum of these particles. Furthermore long living particles that decay after the VELO, for instance K_S^0 's, can be reconstructed using the TT.

3.1.3 Main tracker

The main tracker consists of three Tracking Stations (T-Stations) and each is composed of the Inner Tracker (IT) [13] and the Outer Tracker (OT) [14], see Figure 3.4(a). The Inner Tracker is built around the beam pipe and thus around the region with the largest particle flux. It only covers 2% of the total geometrical acceptance of the T-Stations but it measures 20% of the tracks. Therefore the IT is built of silicon sensors.

The Outer Tracker covers the large area outside the acceptance of the IT. It is built of straw tubes which contain an anode wire and are serving as drift chambers. They are filled with a gas mixture of Ar(70%) and CO₂(30%). The layout can be seen in Figure 3.4(b). The time difference between a pulse at the anode wire and the bunch crossing clock is related to the drift distance of the primary drift electrons in the straw tubes. The read out window of the OT contains three consecutive bunch crossings (75ns) because the maximum drift time of 43 ns and the time delays due to read out electronics needs to be considered. Therefore an additional challenge is to distinguish between so-called spill-over signals from the previous events and signal from the current event. The Inner Tracker and Outer Tracker have, like the TT, modules that are rotated around the z -axis.

The spatial resolution in x -direction is $50\mu m$ for the IT and $200\mu m$ for the OT.

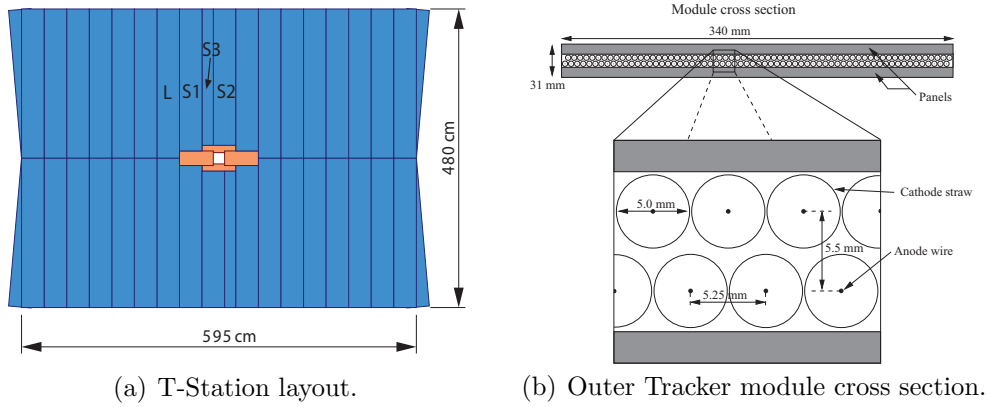


Figure 3.4: (a) Layout of one station of the main tracker. In the inner part the four pads of the inner tracker can be seen. (b) Cross section of an Outer Tracker module. From [15].

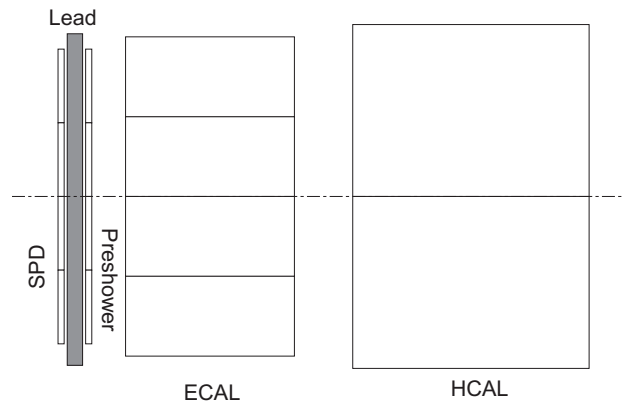


Figure 3.5: Layout of the calorimeter system. Taken from [16].

3.2 Calorimeter system

The Calorimeter system [17] measures energy and position of electrons, photons and hadron. Information from the calorimeter system is used for particle identification and for trigger decisions.

The different components of the calorimeter system can be seen in Figure 3.5. It consists of the Scintillating Pad detector (SPD), the Preshower detector and the electromagnetic (ECAL) and hadronic (HCAL) calorimeters.

Particles interacting with material produce a shower of secondary particles which are finally absorbed in the detector. The particle shower induce ionization in the scintillating detector material and the total amount of scintillation light is proportional to the energy deposition.

The purpose of the SPD is to distinguish charged and uncharged particles, thus it can discriminate electrons and photons. The layer of lead between SPD and Preshower detector initiates an electromagnetic particle shower. Hadronic showers are induced later in the hadronic calorimeter and therefore the Preshower detector is able to distinguish between hadronic and electromagnetic showers.

The electronic calorimeter is built of 66 alternating layers of 2 mmthick lead plates and 4 mmthick plates of scintillating material. It detects shower induced by electrons and photons due to bremsstrahlung and pair production, thus it is the only sub detector that can detect photons. The depth of the ECAL is 25 electromagnetic interaction length¹(X_0) or 1.1 hadronic interaction lengths (λ).

The energy resolution of the ECAL is:

$$\frac{\sigma(E)}{E} = \frac{10\%}{\sqrt{E}} \oplus 1.5\% \quad (3.2)$$

The energy is given in GeV and \oplus denotes a quadratic summation.

The last part of the calorimeter system is the hadronic calorimeter (HCAL). It is built of alternating iron absorbers and scintillating tiles. It is supposed to measure the energy of hadrons. The total depth of the calorimeter is 5.6λ and its energy resolution is:

$$\frac{\sigma(E)}{E} = \frac{80\%}{\sqrt{E}} \oplus 10\% \quad (3.3)$$

¹The electromagnetic interaction length can be approximated by $X_0 = \frac{716.4 \cdot A}{Z(Z+1) \ln \frac{287}{\sqrt{Z}}}$, where Z and A are the atomic number and the mass number of the detector material

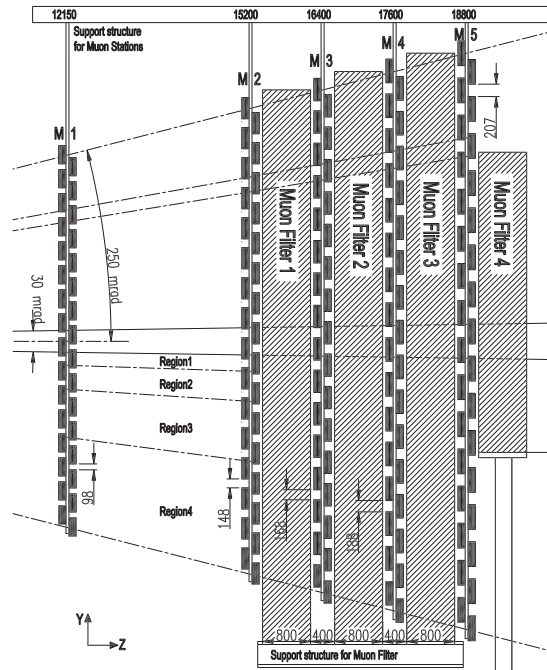


Figure 3.6: Side view of the muon system [18].

with the energy in GeV.

3.3 Muon system

The Muon system [18] consists of five stations (M1-M5). The first muon station is placed in front of the calorimeter system and the others are located behind the hadronic calorimeter. The stations M2 to M5 are separated by iron plates with a thickness of 80cm. The muon system is sketched in Figure 3.6. The material of the muon system corresponds to 20 interaction length and only muons with energies larger than 6 GeV are able to traverse the muon system. The muon stations are equipped with multi-wire proportional chambers (MWPC) which provide a fast readout. This is especially important for the trigger system because the Level 0 trigger requires hits in all five muon stations. In M1 near to the beam pipe GEM detectors are used because of the high particle flux.

3.4 Particle identification system

A good particle identification is a feature of LHCb compared to other LHC experiments. The particle identification system uses information from the Ring Imaging Cherenkov detectors (RICH1 and RICH2) [19], the calorimeter system and the muon chambers in order to identify particles. The RICH detectors are placed before the magnet between VELO and TT (RICH1) and after the magnet between T-Stations and calorimeter system (RICH2). The purpose of the two sub detectors is the identification of particles in different momentum ranges. The RICH1 allows to identify particles which are bent outside the detector acceptance after traversing the magnet. It is supposed to identify particles with momentum smaller than 50 GeV. The RICH2 operates in a momentum range between 50 GeV and 100 GeV.

The basic principle of the RICH detectors is the Cherenkov effect. Light is emitted when a particle traverses a material with refraction index n with a velocity larger than the speed of light in the material $c_{mat} = \frac{c}{n}$ (c is the speed of light in the vacuum). The opening angle Θ_C of the emitted light cone is correlated with the velocity of the particle:

$$\cos(\Theta_C) = \frac{1}{n\beta} = \frac{c_{mat}}{v} \quad (3.4)$$

With the knowledge of the momentum of the particle the mass can be measured.

The information of the RICH detectors is combined with information from other sub detectors in order to assign a relative likelihood for a certain particles hypothesis $\Delta\mathcal{L}_{X-\pi}$ to a track:

$$\Delta\mathcal{L}_{X-\pi} = \log(\mathcal{L}(X)) - \log(\mathcal{L}(\pi)) \quad (3.5)$$

The delta log likelihood $\Delta\mathcal{L}_{X-\pi}$ is always normalized to the pion hypothesis. It is denoted with $DLL_{X-\pi}$ in the following.

3.5 Trigger system

In this section the LHCb trigger system is discussed. The LHCb trigger system is divided into a hardware based low-level trigger(L0) and an software based high

level trigger (HLT). The high level trigger is furthermore divided in two stages (HLT1 and HLT2). The different parts are described in the following.

3.5.1 L0 hardware trigger

At nominal conditions the LHC will have a bunch crossing frequency of 40MHz and the detector will see 14MHz of visible-interactions¹. The level 0 hardware trigger (L0) is supposed to reduce this rate to 1.1 MHz. In general the L0 selects events by transverse momentum and/or transverse energy in the calorimeter. The most important trigger lines are the single- μ , di- μ and the hadron line. In the muon lines events are selected by minimum transverse momentum (single- μ) or minimum sum of the transverse momenta of two muon candidates (di- μ). In order to calculate the momentum a first track estimate is needed. This is done by using hits in the muon chambers. The relative transverse momentum resolution $\frac{\sigma_{P_t}}{P_t}$ is 30% [20]. The hadronic trigger line requires a cluster in the HCAL with a minimum transverse energy. Furthermore the L0 is supposed to reject events with a high multiplicity and/or multiple primary vertices. These events are more difficult to analyze and consume a lot of computing time at later trigger stages. There is also an L0-electron and L0-photon line. For events selected by the L0 trigger the full detector is read out and so in the following trigger stages more information is available.

3.5.2 First stage of the high level software trigger

The first stage of the high level software trigger (HLT1) uses information of the tracking system and a fast track fit is performed. So quantities depending on track parameters can be used to reduce the rate. In general the HLT1 is supposed to confirm the L0 decision. The different trigger lines are shown in Figure 3.7. The trigger lines are executed dependent on the L0 decision.

If an event was triggered by the L0 hadron line. It is processed by the HLT1 single hadron and di-hadron lines. The track estimate from the L0 trigger is improved by using information from the vertex-locator (VELO) and the main tracking system (T-stations). The single-hadron line selects events with a hard p_T cut ($p_T > 5GeV$) on the L0 track. The hard selection criteria is necessary

¹A visible interaction leaves at least 5 tracks in the detector acceptance

to downsize the rate. The di-hadron line looks for a second track which from a good vertex with the L0 track and makes requirements on the second track. The requirements are a minimum impact parameter to the primary vertex ($IP > 0.1mm$) and a minimum transverse momentum ($p_T > 5\text{ GeV}$). In this analysis most of the signal is triggered by hadron lines.

Events triggered by the L0- μ lines are processed by the corresponding HLT1 lines.

3.5.3 Second stage of the high level software trigger

The second stage of the high level trigger (HLT2) is executed on HLT1 filtered events. At nominal conditions the HLT2 is supposed to reduce the rate from approximately 30kHz to the final LHCb trigger output rate of 2kHz. While in the HLT1 only a few tracks are reconstructed the HLT2 performs a full event reconstruction using a fast version of the offline track fit. Afterwards exclusive and inclusive selections are applied.

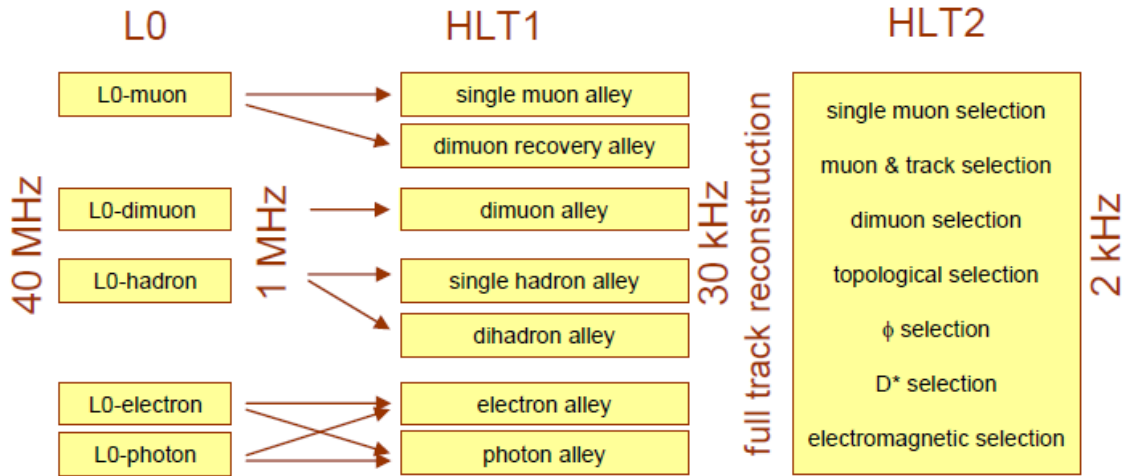


Figure 3.7: The LHCb trigger system. From [20]

Chapter 4

Measurement principle and experimental status

4.1 Measurement principle

To measure $D^0 - \bar{D}^0$ mixing the D^0 flavour at production time and at decay time needs to be determined. The decay via strong interaction $D^{*+} \rightarrow D^0 \pi_{slow}^+$ with the subsequent weak decay of $D^0 \rightarrow K^\pm \pi^\mp$ and the corresponding charge conjugate decay offer the opportunity to tag both the initial and the final state. The charge of the π_{slow} determines the flavour at the production time.

The charges of the D^0 daughter particles determine the D^0 flavour at decay time. The decays with different charge of π_{slow} and kaon are categorized as 'right-sign' decays (RS) and decays with the same charges are 'wrong-sign' decays (WS):

$$\begin{aligned} D^{*+} &\rightarrow D^0 \pi_S^+ \\ &\hookrightarrow D^0 \rightarrow K^- \pi^+ \text{ (RS)} \\ &\hookrightarrow D^0 \rightarrow K^+ \pi^- \text{ (WS)} \end{aligned} \tag{4.1}$$

The RS category is composed of Cabibbo favoured (CF) D^0 decays to the final state $K^- \pi^+$. The Feynman graph for this decay is shown in Figure 4.1(a). The WS event category is either composed of decays where a D^0 has mixed to a \bar{D}^0 with a subsequent CF decay to the final state $K^+ \pi^-$ (Figure 4.1(c)) or of doubly Cabibbo suppressed (DCS) decays to $K^+ \pi^-$ (Figure 4.1(b)).

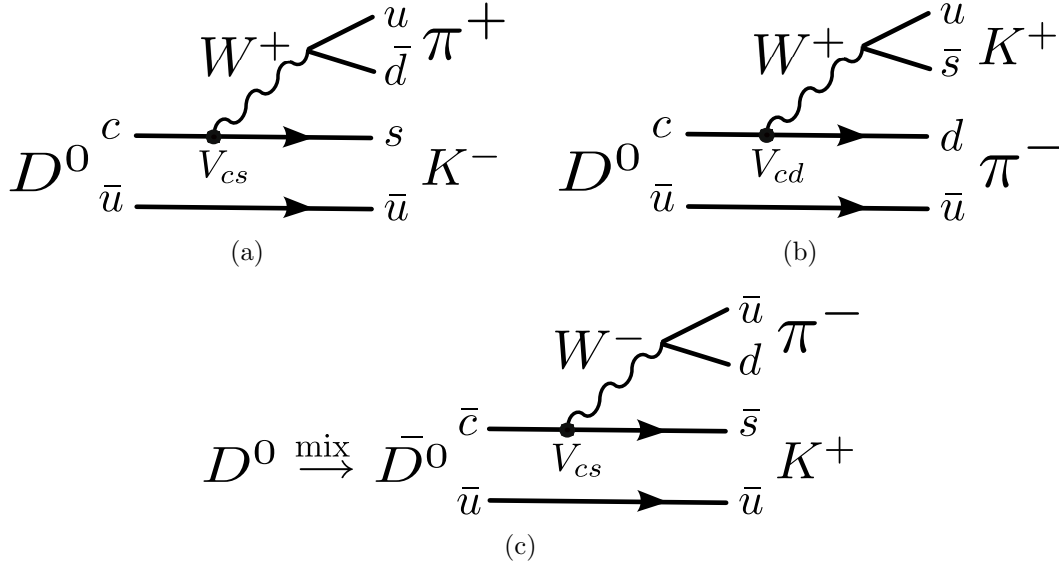


Figure 4.1: Feynman diagrams for (a) Cabibbo favoured D^0 (RS) decays and WS decays. A WS decay is either a D^0 mixed to a \bar{D}^0 with a subsequent CF decay (c) or a doubly Cabibbo suppressed decay (b).

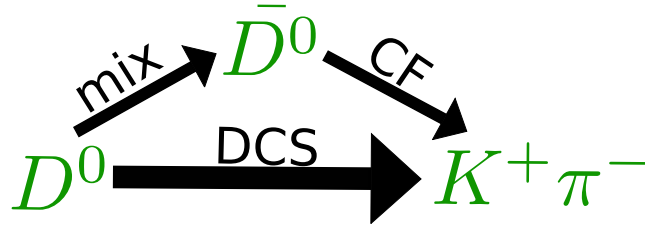


Figure 4.2: Interference between mixing and doubly Cabibbo suppressed decays

The time dependent decay rate distribution for RS events is an exponential function:

$$\Gamma_{RS}(t) \propto e^{-\Gamma \cdot t} \quad (4.2)$$

With the D^0 decay width Γ . For WS events the decay rate is more complicated. It consists of an exponential contribution from DCS and a part from mixing decays. The interference between mixing and DCS decays, as sketched in Figure 4.1, needs to be considered as well. The decay rate for WS events can be approximated by [5]:

$$\Gamma_{WS}(t) \propto e^{-\Gamma \cdot t} \left\{ R_{DCS} + \sqrt{R_{DCS}} \cdot y' \cdot t + \frac{x'^2 + y'^2}{4} \cdot t^2 \right\} \quad (4.3)$$

The factor $R_{DCS} = r_d^2 \approx 3 \cdot 10^{-3}$ is the ratio of the decay amplitudes of the Cabibbo favoured and the doubly Cabibbo suppressed decay. The value measured by BaBar [1] is $R_{DCS} = 3.03_{\pm 0.16(stat)}^{\pm 0.1(sys)} \times 10^{-3}$. The contribution from the mixing amplitude is proportional to t^2 . The mixing parameters x' and y' which appear in the expression consider the additional phase difference δ_f between CF and DCS decays (see Equation 2.9):

$$x' = x \cdot \cos(\delta_f) \quad y' = y \cdot \cos(\delta_f) \quad (4.4)$$

As a consequence, the measurement of the time dependent decay rate of WS events, allows a determination of the mixing parameters only up to the phase δ_f . This phase was measured by CLEO [21]: $\cos(\delta_f) = 1.03_{-0.17}^{+0.31}(stat) \pm 0.06(sys)$.

The term $\propto t$ in Equation 4.3 describes the interference between DCS decay and mixing.

The mixing parameters can be extracted from the time dependence of the WS decay rate. To extract the mixing parameters either the time dependence of the decay time is fit directly according Equation 4.3, or the ratio $R(t)$ of time dependent WS and RS decay rates is used. This ratio is given by:

$$R(t) = \frac{\Gamma_{WS}(t)}{\Gamma_{RS}(t)} = R_{DCS} + \sqrt{R_{DCS}} \cdot y' \cdot t + \frac{x'^2 + y'^2}{4} \cdot t^2 \quad (4.5)$$

To measure $R(t)$ a binned approach is used. In time bins Δt_i of the D^0 lifetime the ratio between $WS(N_{WS})$ and $RS(N_{RS})$ events calculable:

$$R(\Delta t_i) = \frac{N_{WS}(\Delta t_i)}{N_{RS}(\Delta t_i)} \quad (4.6)$$

The measurement of the decay time dependent decay rate of WS events (1st method) requires and well known acceptance correction of the D^0 lifetime distribution. In the 2nd method detector acceptances do not change the value of $R(\Delta t_i)$, because RS and WS events have the same kinematics and thus they are effected in the same way. Nevertheless acceptance effects have to be studied because they lead to a lower number of events at low lifetimes and thus the error of the mixing parameters are influenced. This is shown in Chapter 6.5 and 8.2.

D^* 's can either be produced in B decays or directly in a $c\bar{c}$ event. The production rate for directly produced D^* 's is much higher than for D^* 's from B decays.

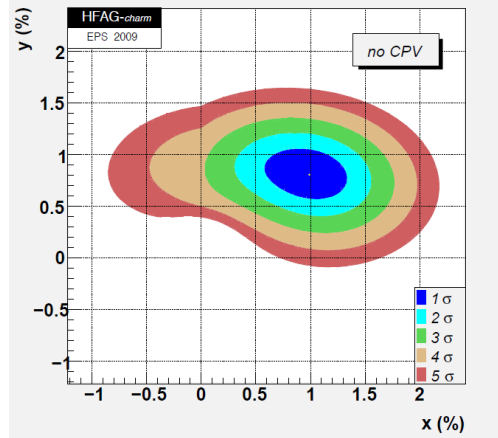


Figure 4.3: HFAG result [23] for the D^0 mixing parameters. It is assumed that there is no \mathcal{CP} violation.

Furthermore D^{*} 's have a very short lifetime ($\tau_{D^*} \sim \mathcal{O}(10^{-24} \text{s})$) and for D^{*} 's originating from the primary vertex the primary vertex can be used as decay vertex of the D^* and thus as production vertex of the D^0 . The primary vertex can be measured precisely and the D^0 lifetime resolution is good for these events. For these reasons prompt D^{*} 's are used in this work.

4.2 Experimental status

Evidence for $D^0 - \bar{D}^0$ mixing was found by the BaBar [1], CDF [2] and Belle [22] collaborations. The currently best estimate for the mixing parameters a and y by the Heavy Flavour Averaging Group (HFAG) is shown in Figure 4.3. It combines the result of several experiments in a global fit procedure. The no-mixing ($x = y = 0$) case is excluded at 10.2σ [23]. However a 5σ measurement of a single experiment is currently not available. In the following I will shortly discuss the results from BaBar and CDF.

BaBar is a e^+e^- collider, located at SLAC National Accelerator Laboratory, and collected a set of ≈ 4000 WS decays. The decay time distribution for WS events is shown in Figure 4.4(a). The mixing parameters were extracted using an unbinned maximum likelihood fit to this distribution. The WS decay time function is given in 4.3. The analysis provide evidence for $D^0 - \bar{D}^0$ mixing at a level of 3.9 standard deviations [1]. No evidences for \mathcal{CP} violation were found.

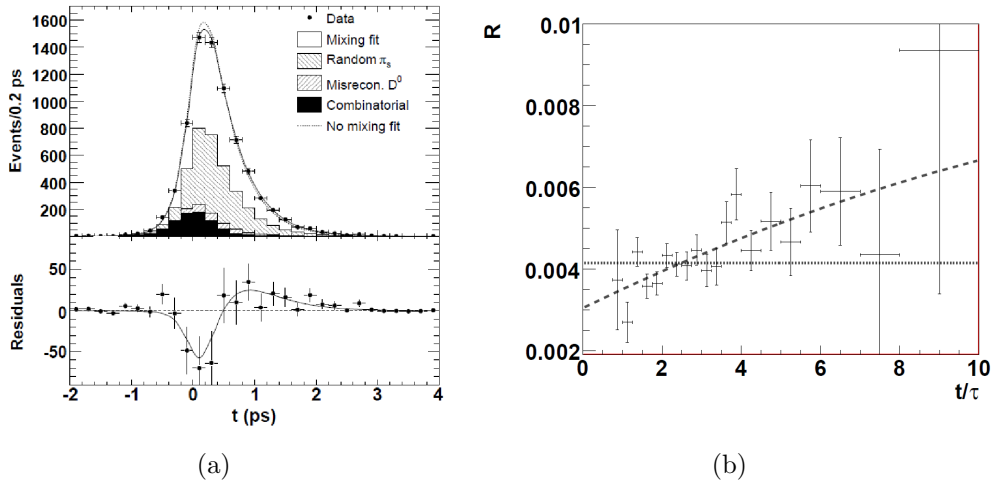


Figure 4.4: (a) In the upper part the BaBar lifetime distribution for 'wrong-sign' events is shown [1]. The mixing and no-mixing fit are shown by the solid and dashed curves. The residuals of the data points w/r to the no mixing case and the expectation for the mixing scenario (solid line) are shown below. (b) The ratio $R(\Delta t) = N_{WS}(\Delta t)/N_{RS}(\Delta t)$ as measured by CDF with the fits for the mixing (long dashed) and no-mixing (short dashed) case are shown [2].

The CDF experiment operates, like LHCb at a hadron collider. It is located at the Tevatron accelerator at Fermilab. It is still collecting data and the analysis [2] was performed using ≈ 13000 WS decays. The mixing parameters were measured by a binned fit of the ratio $R(\Delta t) = \frac{N_{WS}(\Delta t)}{N_{RS}(\Delta t)}$. The result is shown in Figure 4.4(b). CDF was able to exclude the no mixing scenario at a level of 3.8 [2] standard deviations.

Chapter 5

Monte Carlo simulation

This chapter describes the LHCb Monte Carlo data samples used in this work. The simulation is done in two phases by the *Gauss* v37r2 [24] software framework. In the first phase pp collisions are simulated using the external program *PHYTIA* v6.418 [25]. In the second phase the propagation of the particles through the detector and the corresponding energy loss is simulated using the *Geant4* [26] package. Afterwards the responses of the various sub detectors are simulated by *Boole* [27].

5.1 Signal sample

The signal sample¹ is an inclusive sample of the decay $D^{*+} \rightarrow D^0 \pi_{slow}^+ \rightarrow \{hh\} \pi_{slow}^+$ and its charge conjugate. The final state hadrons can be pions or kaons. It includes prompt D^* as well as D^* from B decay. The sample was generated with a center of mass energy of 10 TeV and corresponds to an integrated luminosity of 0.62 pb^{-1} . The luminosity is given by:

$$\mathcal{L} = \frac{\# \text{ events}}{\epsilon_{gen}} \left(\{ \sigma_{bb} f_{b \rightarrow B} f_{B \text{ accepted}} \mathcal{B}_{B \rightarrow D^*} + \sigma_{cc} f_{c \rightarrow D^*} f_{D^* \text{ accepted}} \} \mathcal{B}_{D^* \rightarrow D^0 \pi_S \rightarrow \{K\pi\} \pi_S} \right)^{-1} \quad (5.1)$$

Every event is required to have a D^* with a momentum pointing into the detector acceptance. The fraction of these events with respect to all generated D^* events is given by ϵ_{gen} . The cross sections for $b\bar{b}$ and $c\bar{c}$ production are given by σ_{bb} and

¹LHCb event type number: 27363001 (Dst_D0pi,hh=DecProdCut)

Quantity	Value
ϵ_{gen}	0.41 ± 0.002
σ_{bb}	$0.7 \pm 0.01 mb$
σ_{cc}	$6.26 \pm 0.01 mb$
$f_{B^{accepted}}$	0.786 ± 0.017
$f_{D^{*accepted}}$	0.7324 ± 0.002451
$f_{b \rightarrow B}$	0.798 ± 0.015
$f_{c \rightarrow D^*}$	0.255 ± 0.017
$\mathcal{B}_{B \rightarrow D^*}$	0.225 ± 0.015
$\mathcal{B}_{D^* \rightarrow D^0 \pi_S \rightarrow \{K\pi\} \pi_S}$	0.03 ± 0.004

Table 5.1: Generation values for the signal Monte Carlo sample. Branching fractions taken from [28].

σ_{cc} , $f_{b \rightarrow B}$ and $f_{c \rightarrow D^*}$ describe the probability to form a B or a D* respectively. The fractions of accepted B and D* mesons are given by $f_{B^{accepted}}$ and $f_{D^{*accepted}}$ and \mathcal{B}_X are the branching fraction from [28]. The used values are listed in Table 5.1.

5.2 Minimum bias sample

The so-called 'minimum bias' sample contains events with at least one proton-proton interaction. The corresponding integrated luminosity is given by:

$$\mathcal{L} = \frac{\# \text{ events}}{\sigma_{pp} f_{accept}} \quad (5.2)$$

The fraction of events with at least one proton-proton interaction is given by f_{accept} . The Monte Carlo data was generated with in average one proton-proton interaction per event. The number of interactions is Poisson distributed and the fraction with at least one interaction f_{accept} is $1 - \frac{1}{e}$. For the proton-proton cross section $\sigma_{pp} = 100 \text{ mb}^{-1}$ is used.

There are 10^9 simulated events available. For technical reasons the events used here have passed a filter process. Only events that probably will be selected by the hardware trigger (L0) and the first stage of the software trigger (HLT1) are used. After the filtering there are 24×10^6 events remaining. The minimum bias sample is especially used to estimate the expected amount of combinatoric background (see Chapter 10).

Chapter 6

Selection

This chapter describes the selection of the decay $D^{*+} \rightarrow D^0 \pi_S^+ \rightarrow \{K\pi\} \pi_S^+$ and its charge conjugate decay. In the following the selection and the used quantities are discussed.

A preselection is applied to the Monte Carlo signal sample. It consists of a set of momentum and particle identification criteria (see Table 6.1) and it requires that all candidates were selected by the L0 and HLT1 trigger stages.

As shown in Chapter 10 the background will later be determined by a two dimensional fit to the invariant mass of the D^0 combination (M_{D^0}) and Δm . Whereas the mass difference between invariant mass of the D^* combination and the invariant masses of D^0 and π_S is denoted as Δm :

$$\Delta m = M_{D^*} - M_{D^0} - M_{\pi} \quad (6.1)$$

In order to be able to determine the amount of background the sidebands of the distributions are needed and therefore large windows for M_{D^0} and Δm are chosen. The preselection has a signal efficiency¹ of $(79 \pm 1)\%$.

The selection is a set a criteria with the purpose to select WS and RS events with a reasonable amount of background. WS events have a branching fraction which is three orders of magnitude smaller than the branching fraction for RS events and a large combinatoric background from prompt kaons and pions is expected. These kaons and pions are produced in the hadronization process, thus their origin is the primary vertex, which is also the origin of the D^0 . Therefore

¹The signal efficiency is defined as: $\epsilon_{sig} = \frac{\# \text{candidates after selection}}{\# \text{candidates before selection}}$

Particle	Selection quantity	Selection value
D^0 daughters (K, π)	$p(K, \pi)$	> 12 GeV (5 GeV)
	$DLL_{K-\pi}(\pi)$	< 0
	$DLL_{K-\pi}(K)$	> 8 (-5)
	$track \chi^2/ndf(K, \pi)$	< 2
D^0	$p(D^0)$	> 40 GeV (10 GeV)
	$p_T(D^0)$	> 5 GeV (2 GeV)
	$DIRA(D^0)$	> 0.99997
	$fDSig$	> 7
	$cos(\xi)$	< -0.965
	$vertex \chi^2/ndf(D^0)$	< 5
π_S	$p_T(\pi_S)$	> 350 MeV
	$IP(\pi_S)$	< 0.15 mm
	$DLL_{K-\pi}(\pi_S)$	< -2.5
	$track \chi^2/ndf(\pi_S)$	< 2
D^*	$IP(D^*)$	< 0.035 mm
	$vertex \chi^2/ndf(D^*)$	< 5
$\Delta m < 50.5$ MeV		
1764.8 MeV $< M_{D^0} < 1964.8$ MeV		

Table 6.1: Selection criteria for the different particles. Values of the preselection are given in brackets.

selecting WS events is not a trivial task.

WS and RS events are kinematically identical and one can expect that the different backgrounds have the same shape for WS and RS events. However, in some background categories the relative contribution differs between WS and RS as will be discussed in Chapter 7. Therefore the distributions shown in this chapter contain WS events because they are more difficult to select. For every selection criterion two distributions are shown, one for signal and background after the preselection and the second with all but the shown selection criterion applied. The latter are called N-1 distributions in the following. This technique allows to choose an optimal value given all other criteria. The selection values are indicated in the various distributions.

A summary of all selection criteria is presented in Table 6.1. Three different categories are distinguished in the following: kinematic selection quantities, particle identification and selection quantities based on the vertex and track quality.

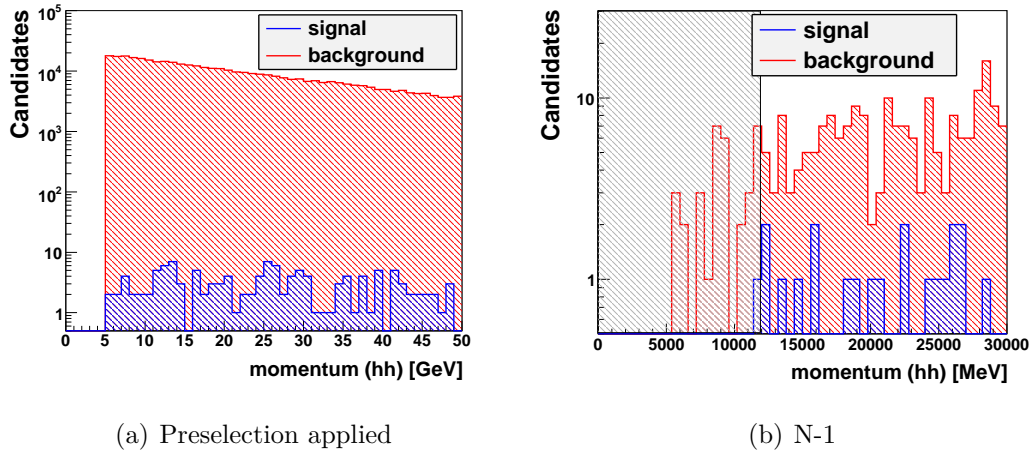


Figure 6.1: Momentum of D^0 daughter particles for signal (blue) and background (red).

6.1 Kinematic selection quantities

6.1.1 Momentum

The transverse momentum (p_T) is the momentum component perpendicular to the axis along the beam pipe (z -axis). In Chapter 3 the momentum measurement is described.

The distribution of the momentum of the D^0 daughter particles is shown in Figure 6.1 for signal and background candidates. Background candidates tend to have small momenta while the momentum spectrum for signal events is flat. The selection chooses candidates with a momentum larger than 12 GeV. The N-1 distribution in Figure 6.1(b) shows that this is a good value, given all other selection criteria.

Distributions of momentum (p) and transverse momentum (p_T) of the D^0 are shown in Figure 6.2 and Figure 6.3. The background candidates have smaller values of p and p_T as the signal. Candidates with a D^0 momentum larger than 40 GeV and a D^0 transverse momentum larger than 5 GeV are selected.

The transverse momentum distribution of the π_S is shown in Figure 6.4. Candidates with a transverse momentum p_T larger than 350 MeV are selected.

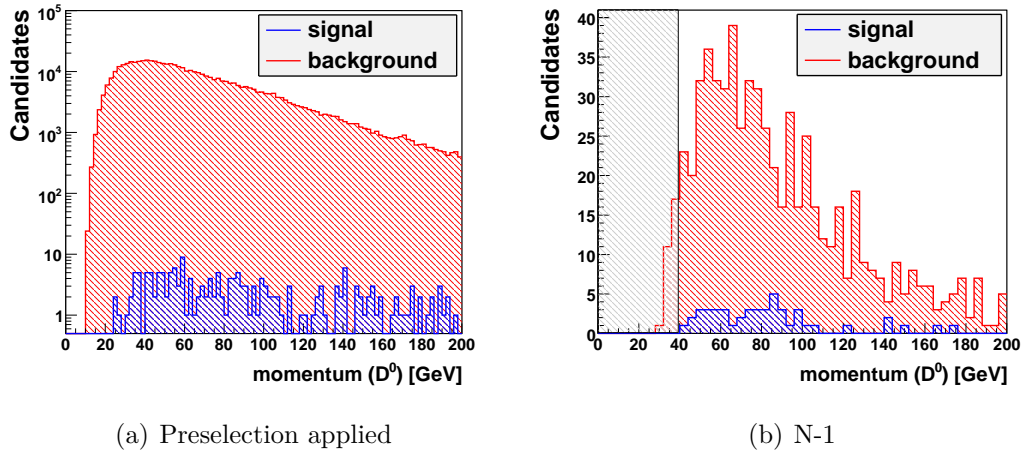


Figure 6.2: Momentum of D^0 for signal (blue) and background (red).

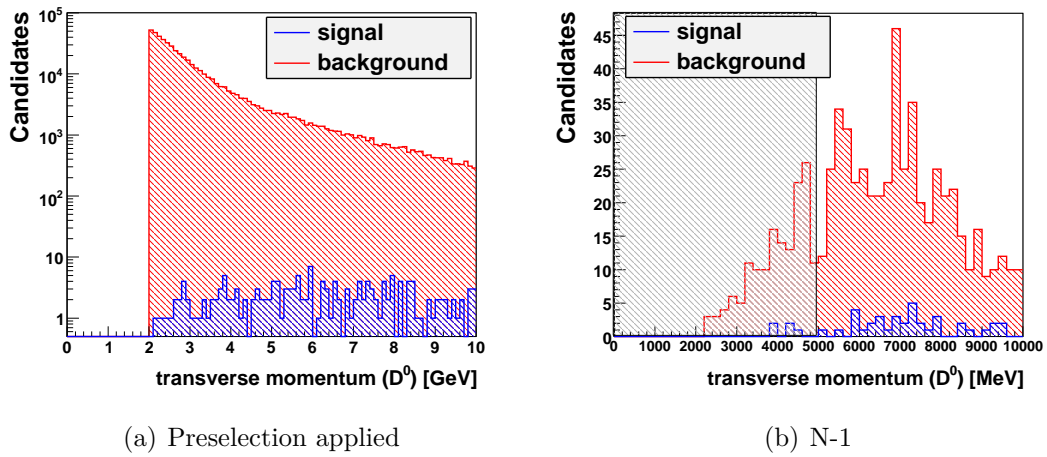


Figure 6.3: Transverse momentum of D^0 for signal (blue) and background (red).

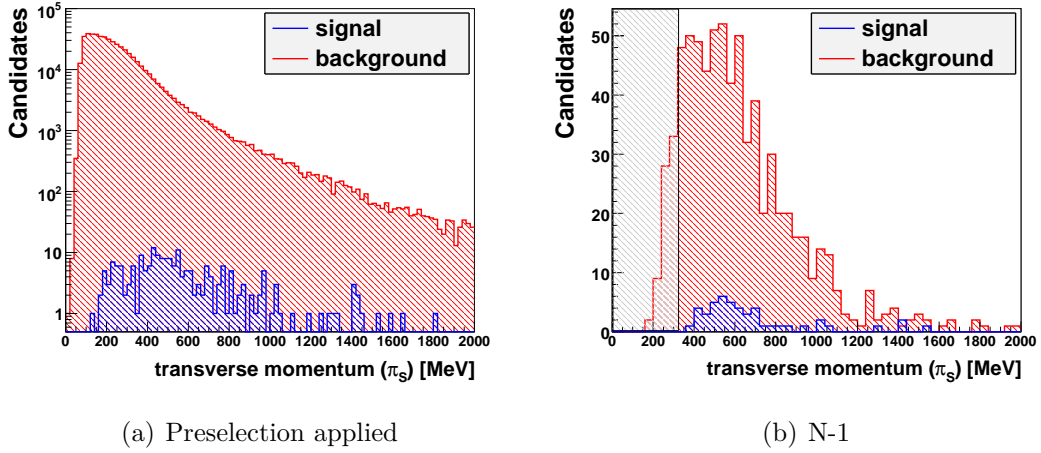


Figure 6.4: Transverse momentum of π_S for signal (blue) and background (red).

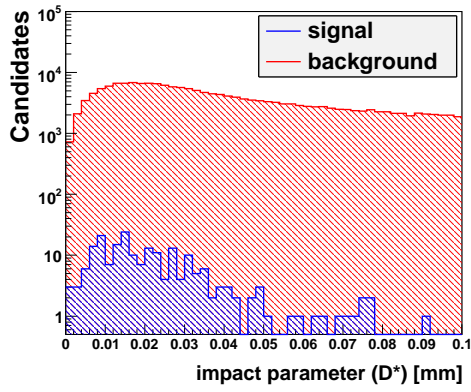
6.1.2 Impact parameter

The impact parameter (IP) of a track and a vertex is defined as the smallest distance between track and vertex. The vertex is in this scope always the primary vertex. In case of multiple primary vertices the reconstruction software uses the vertex with the smallest impact parameter. Figure 6.5 and Figure 6.6 show distributions of the D^* and the π_S impact parameter for signal and background. The shapes of signal and background are similar in the N-1 plots, thus the separation power is limited. Candidates with a D^* impact parameter smaller than 0.035mm and a π_S impact parameter smaller than 0.15mm pass the selection. Another selection criterion that one could think about is the D^0 impact parameter. As there is a large correlation with the D^* impact parameter there is no additional separation power for this variable.

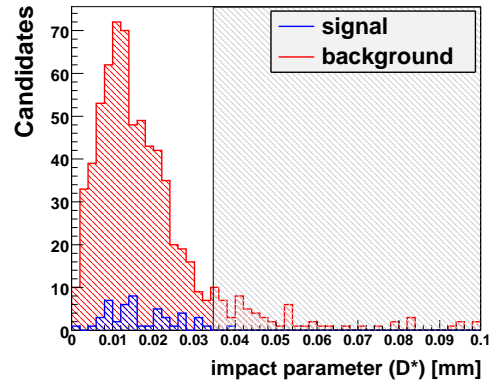
6.1.3 Flight distance significance

The flight distance significance (fDSig) is the distance between production and decay vertex of the D^0 divided by the error of the distance measurement:

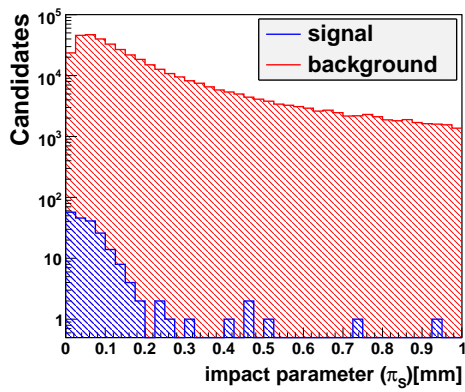
$$\text{fDSig} = \frac{\text{flight distance}}{\text{error of flight distance}} \quad (6.2)$$



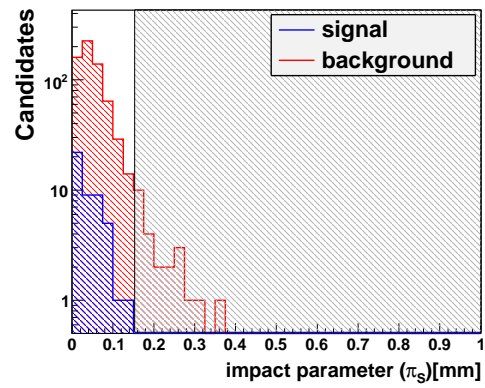
(a) Preselection applied



(b) N-1

Figure 6.5: D^* impact parameter for signal (blue) and background (red).

(a) Preselection applied



(b) N-1

Figure 6.6: π_s impact parameter for signal (blue) and background (red).

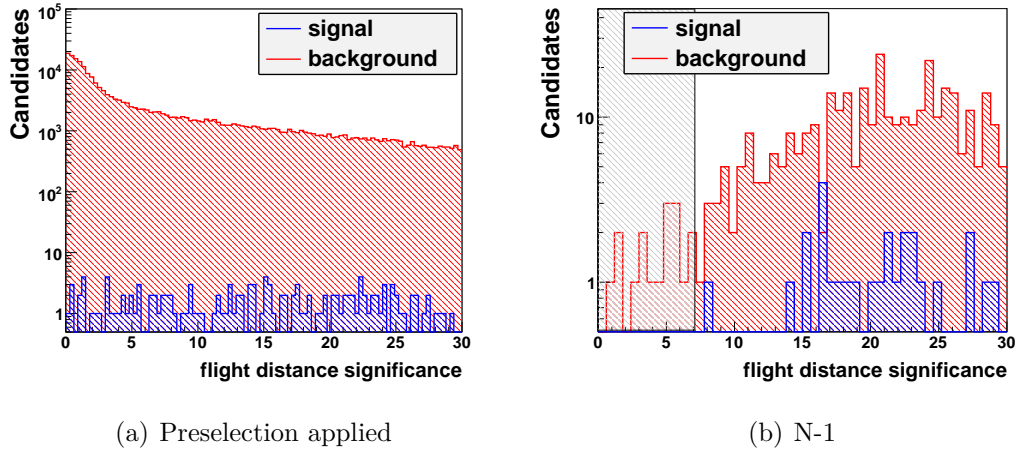


Figure 6.7: Flight distance significance (fDSig) of the D^0 for signal (blue) and background (red).

As production vertex the primary vertex is used. The lifetime of a particle is calculated using the flight distance and the momentum, thus it is expected that the selection quantity fDSig influences the measurement of the D^0 lifetime. Nevertheless, this selection quantity is needed to suppress background from prompt kaons and pions. Choosing the fDSig selection value balances between a smaller background contribution or a less distorted D^0 lifetime distribution

Distributions of fDSig for signal and background are shown in Figure 6.7. Candidates with fDSig larger than 7 are chosen. It can be seen in Figure 6.7(b) that this is a conservative choice. The influence on the lifetime distribution of the D^0 is discussed in 6.5.

6.1.4 Pointing variables

In order to select prompt D^* candidates, we need to separate the signal from secondary D^* e.g. from B decays. The pointing variables DIRA and $\cos(\xi)$ are illustrated in Figure 6.8 and their purpose is to select candidates originating from the primary vertex.

The direction angle α is the angle between the D^0 flight direction and the connection line between D^0 decay vertex and primary vertex. The cosine of the direction angle is denoted by DIRA. A small angle corresponds to particles com-

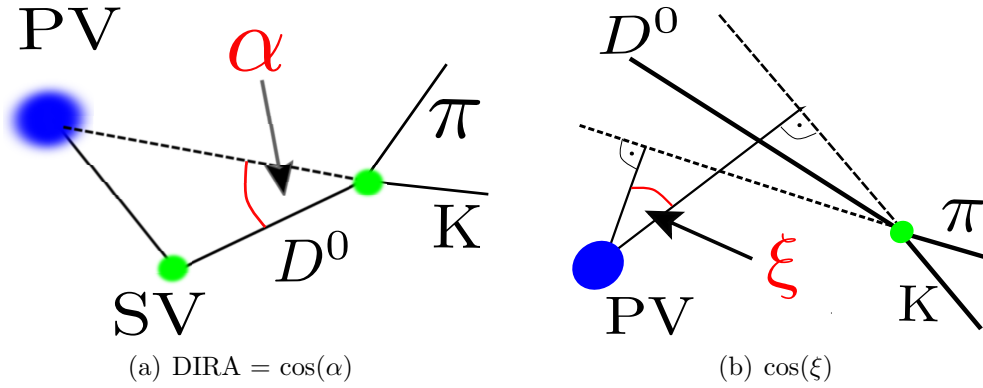


Figure 6.8: Illustration of the pointing variables.

ing from the primary vertex (Figure 6.8a). The distributions for signal and background are shown in Figure 6.9(a). Candidates with DIRA larger than 0.99997 are chosen. The separation power is small but because of some background candidates at small values a wide background distribution can be expected.

Another pointing variable is $\cos(\xi)$. ξ is the angle between the normal vectors on the D^0 daughter tracks (K, π) through the primary vertex as shown in Figure 6.8(b). This quantity is sensitive on the pointing of the D^0 momentum back to the primary vertex as well as on the opening angle of the D^0 daughters. For prompt signal candidates the angle is large, thus $\cos(\xi)$ for signal is around -1 . Figure 6.10 shows the $\cos(\xi)$ distributions for signal and background. The selection chooses candidates with $\cos(\xi)$ smaller than -0.965 .

The quantities DIRA and $\cos(\xi)$ are, like $fDSig$, correlated with the D^0 lifetime, see Section 6.5.

6.2 Particle identification

Quasi stable particles are identified by the two Ring Imaging Cherenkov detectors (RICH1 and RICH2). The particle identification at LHCb is covered in Chapter 3.4. For every quasi stable particle a likelihood for a certain particle hypothesis is formed. We select candidates on the likelihood difference of the kaon and pion hypothesis ($DLL_{K-\pi}$), see Equation 3.5. A particle with a large $DLL_{K-\pi}$ denotes a high probability that the particle is a kaon. Small (negative) values indicate pions.

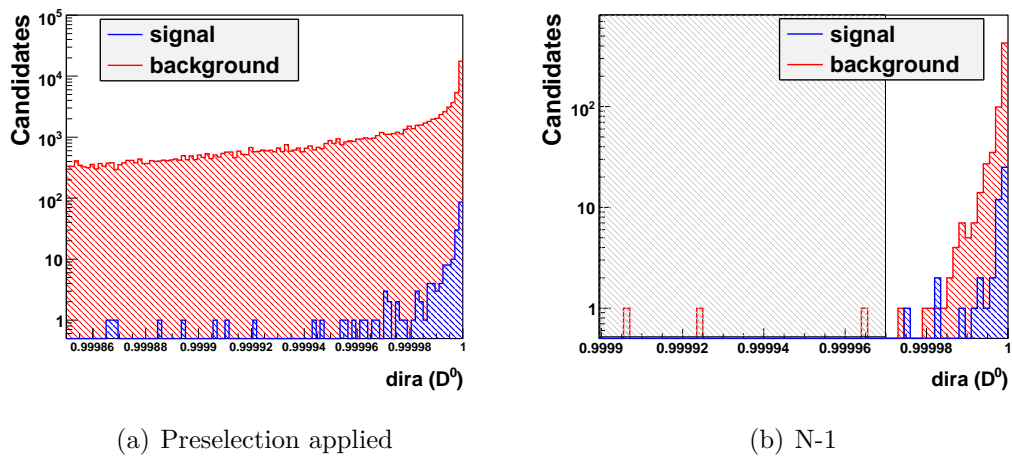


Figure 6.9: DIRA of D^0 for signal (blue) and background (red).

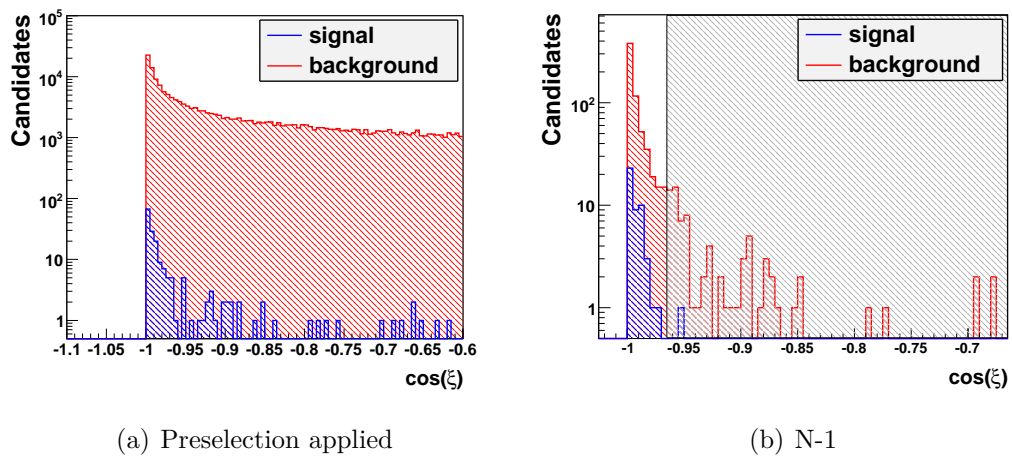


Figure 6.10: $\cos(\xi)$ of D^0 for signal (blue) and background (red).

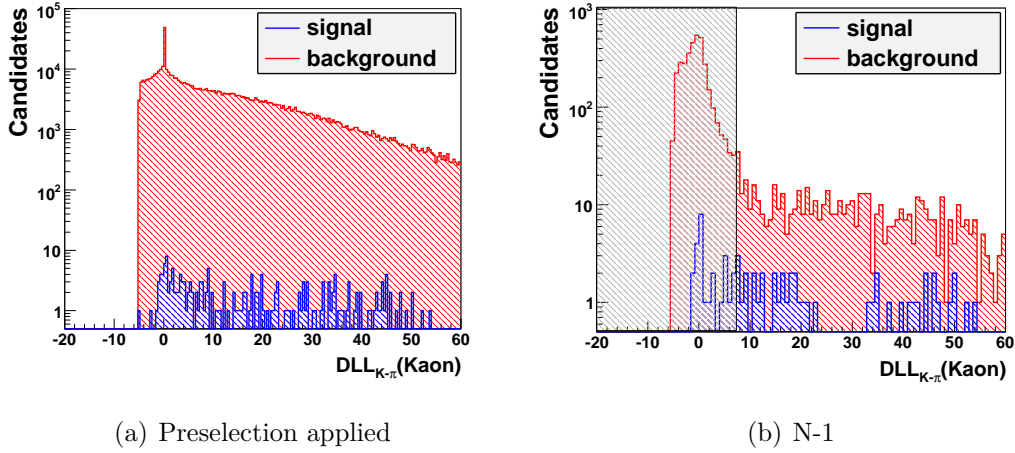


Figure 6.11: $DLL_{K-\pi}$ for kaons for signal (blue) and background (red).

Distributions for D^0 daughter particles and π_S are shown in Figures 6.11, 6.12 and 6.13. The selection requires kaons with a $DLL_{K-\pi}$ larger than 8 and pions with $DLL_{K-\pi}$ smaller than 0 to form D^0 candidates. These are combined with pions whose $DLL_{K-\pi}(\pi_S)$ is smaller than -2.5 to reconstructed D^* candidates.

6.3 Track and vertex quality

To obtain the track parameters of a quasi stable particle the hits from the main tracker and vertex locator (VELO) are used. The LHCb tracking system is described in Chapter 3.

The χ^2/ndf of a track gives the quality of the track fit. In Figure 6.14 and 6.15 the distributions of track χ^2/ndf for the D^0 daughter particles and for the π_S are shown. Both D^0 daughter particles enter the distribution in Figure 6.14. For signal candidates the track χ^2/ndf is around 1. A separation of signal and background is not possible. The selection requires for D^0 daughters and the π_S a χ^2/ndf smaller than 2.

The D^0 and D^* vertices are determined by a vertex fit of the daughter tracks. The χ^2/ndf distributions of the D^0 and D^* vertex fit are shown in Figure 6.16 and 6.17. For the D^0 and the D^* vertex a χ^2/ndf smaller than 5 is required.

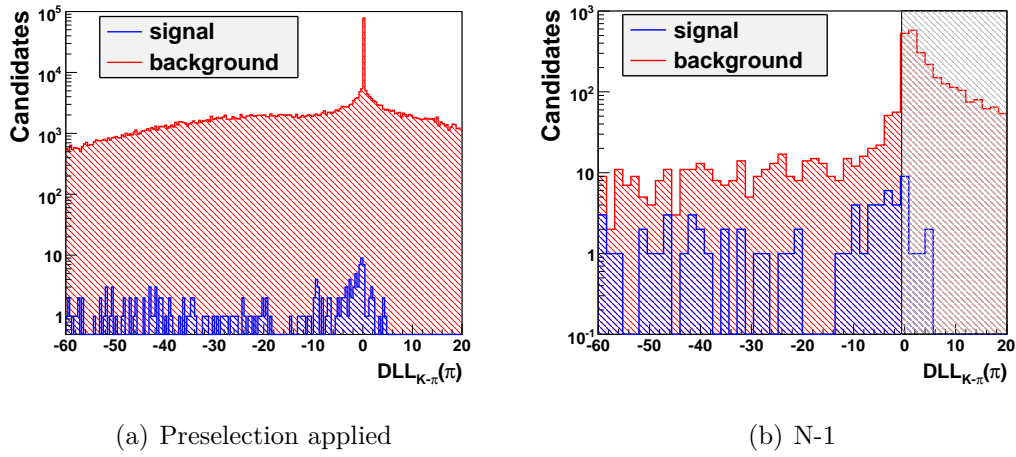


Figure 6.12: $DLL_{K-\pi}$ for pions for signal (blue) and background (red).

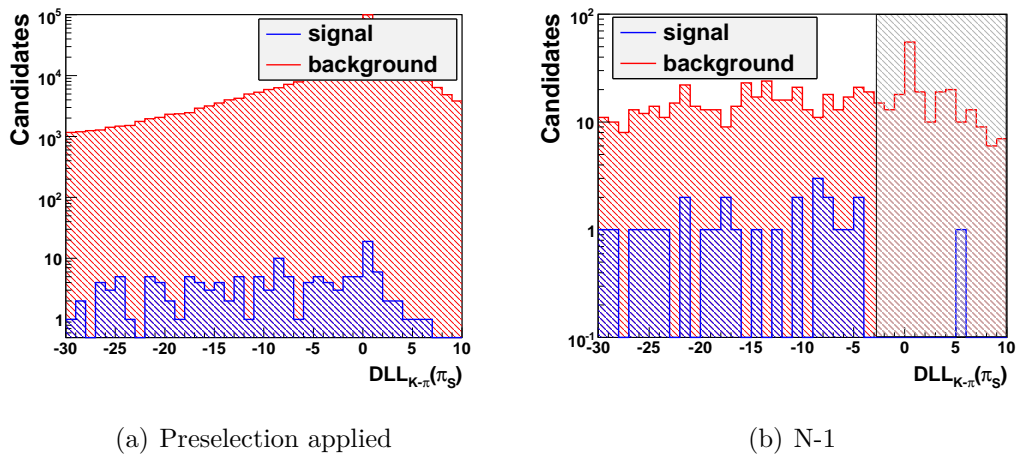


Figure 6.13: $DLL_{K-\pi}$ for π_S for signal (blue) and background (red).

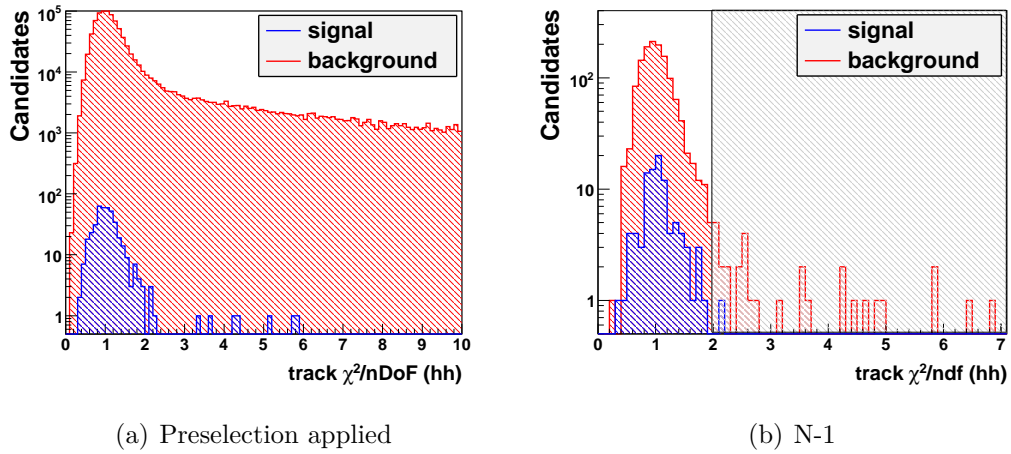


Figure 6.14: Quality of D^0 daughter tracks for signal (blue) and background (red).

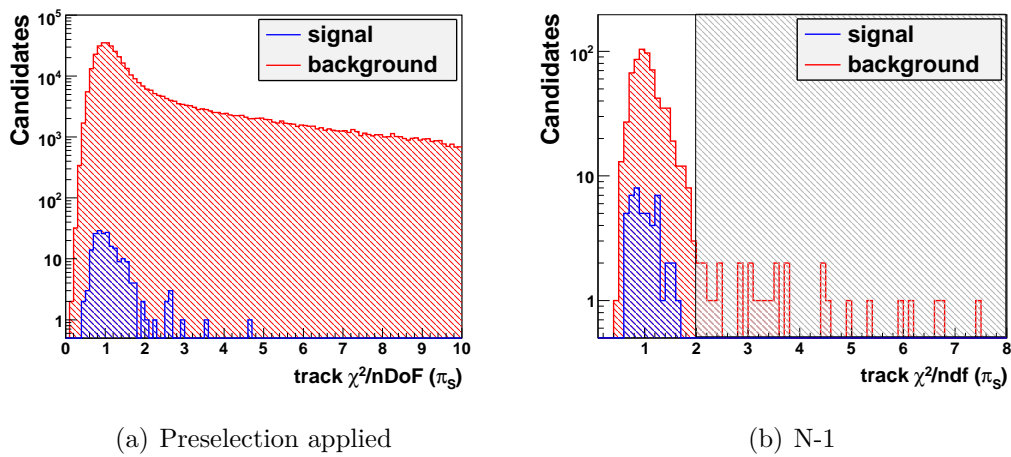


Figure 6.15: Quality of π_S track for signal (blue) and background (red).

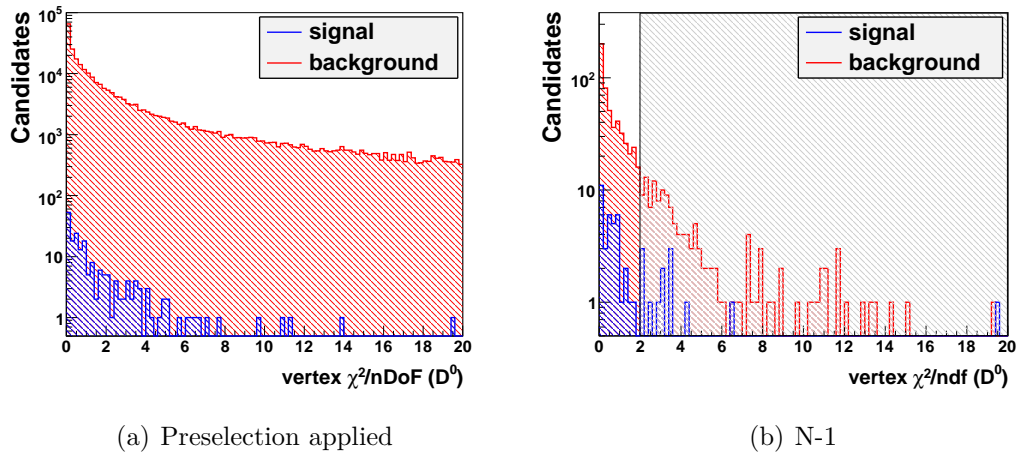


Figure 6.16: Quality of D^0 vertex for signal (blue) and background (red).

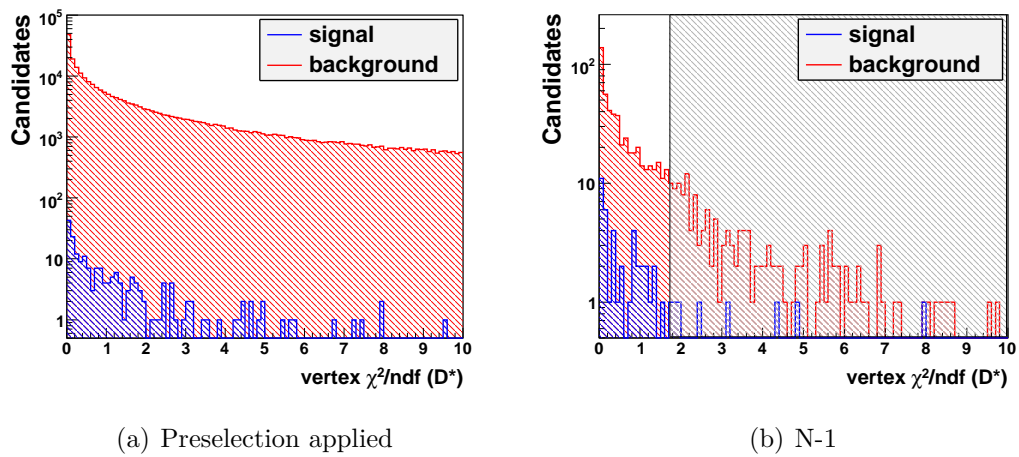


Figure 6.17: Quality of D^* vertex for signal (blue) and background (red).

6.4 Selection results

The efficiency of every single selection requirement is listed in Table 6.2. Two quantities are defined:

$$\epsilon_i = \frac{\text{\#candidates after criterion}_i \text{ applied}}{\text{\#candidates after preselection}} \quad (6.3)$$

$$\epsilon_i^{N-1} = \frac{\text{\#candidates after selection applied}}{\text{\#candidates after Selection without cut}_i}$$

The efficiencies are calculated for signal and background. The previous diagrams contain WS candidates and the selection was optimized for the ratio of WS signal candidates over background (S_{WS}/B) but because of the low statistics of WS candidates the efficiencies were calculated using RS candidates. Contrary to the relative amount of background which differs for RS and WS these efficiencies are the same for RS and WS. Table 6.2 shows that all selection criteria are useful. It can easily be seen that the requirements on the particle identification are most effective. The momentum of the D^0 daughters and the $\cos(\xi)$ quantity are also important criteria.

The total selection efficiency¹ is $(1.84 \pm 0.04)\%$. The background will be studied in Chapter 7.

6.5 D^0 lifetime dependence on selection

It is expected that the selection introduced in this chapter distorts the D^0 lifetime measurement because it has a non-uniform lifetime acceptance. The selection criteria fDSig, DIRA and $\cos(\xi)$ are correlated to the D^0 lifetime and the requirements in these variables favour candidates with large D^0 lifetimes. Thus, the D^0 lifetime distribution has less candidates at small lifetimes than expected from an exponential distribution. This effect is shown in Figure 6.18. Shown is the lifetime acceptance with a trick. The diagram has an exponentially increasing bin width ($\propto e^{t/\tau_{D^0}}$) and an undistorted exponential distribution would result in a constant, as can be seen at lifetimes > 1 ps.

The values that were chosen for the fDSig and $\cos(\xi)$ selection criteria are a conservative choice. Harder criteria can improve the level of background after the

Selection criterion	signal loss	background suppression	signal loss N-1	background suppression N-1
	$1 - \epsilon_i^{sig}$ [%]	$1 - \epsilon_i^{bg}$ [%]	$1 - \epsilon_i^{N-1 sig}$ [%]	$1 - \epsilon_i^{N-1 bg}$ [%]
$p(K, \pi) > 12GeV$	17.24 ± 0.16	43.10 ± 0.07	8.34 ± 0.29	43.6 ± 1.2
$DLL_{K-\pi}(\pi < 0, K > 8)$	35.37 ± 0.20	68.32 ± 0.07	41.92 ± 0.41	86.0 ± 0.4
$track \chi^2/ndf(K, \pi) < 2$	7.35 ± 0.11	37.96 ± 0.07	3.13 ± 0.17	21.5 ± 1.2
$p(D^0) > 40GeV$	12.01 ± 0.14	25.16 ± 0.06	2.07 ± 0.15	15.2 ± 1.0
$p_T(D^0) > 5GeV$	27.83 ± 0.19	86.94 ± 0.05	5.26 ± 0.24	32.1 ± 1.2
$DIRA(D^0) > 0.99997$	19.67 ± 0.17	88.37 ± 0.04	0.61 ± 0.08	5.0 ± 0.7
$fDSig > 7$	19.26 ± 0.17	67.69 ± 0.06	1.57 ± 0.13	11.9 ± 1.0
$\cos(\xi) < -0.965$	32.95 ± 0.20	86.48 ± 0.05	10.07 ± 0.31	48.8 ± 1.1
$vertex \chi^2/ndf(D^0) < 5$	9.34 ± 0.13	54.91 ± 0.07	4.78 ± 0.22	30.0 ± 1.2
$p_T(\pi_S) > 350MeV$	24.81 ± 0.19	78.92 ± 0.06	2.46 ± 0.17	17.6 ± 1.1
$IP(\pi_S) < 0.15mm$	13.73 ± 0.15	57.36 ± 0.07	1.54 ± 0.13	11.7 ± 1.0
$DLL_{K-\pi}(\pi_S) < -2.5$	27.22 ± 0.19	73.26 ± 0.06	13.17 ± 0.34	56.3 ± 1.0
$track \chi^2/ndf(\pi_S) < 2$	6.30 ± 0.10	42.00 ± 0.07	2.56 ± 0.17	18.2 ± 1.1
$IP(D^*) < 0.035mm$	15.12 ± 0.15	82.52 ± 0.05	2.99 ± 0.18	20.8 ± 1.1
$vertex \chi^2/ndf(D^*) < 5$	9.43 ± 0.13	53.65 ± 0.07	4.64 ± 0.22	29.3 ± 1.2

Table 6.2: Selection efficiencies.

selection but it also increases the effect on the lifetime distribution. A distorted lifetime measurement is not expected to change the value of the mixing parameters (see 'ratio' method in Section 4.1). But because of less signal candidates at low lifetimes the errors of the mixing parameters are expected to be larger.

It still needs to be studied if a cleaner sample or a larger number of events at small lifetimes gives the best error on the mixing parameters. A further distortion of the lifetime measurement is caused by the trigger, see Chapter 8.2. Both effects are studied in Chapter 11 using a simplified Monte Carlo simulation.

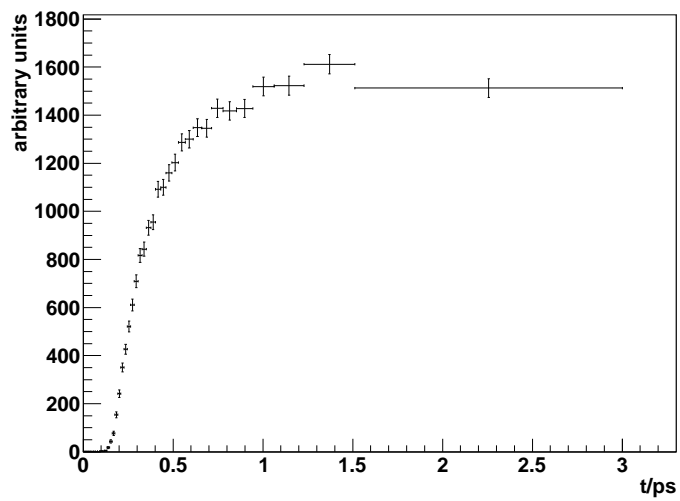


Figure 6.18: D^0 lifetime distribution with an exponentially increasing bin width. The D^0 lifetime distribution is influenced up to approximately 1 ps

Chapter 7

Background

In the following chapter the different types of background contributions to the decay $D^{*+} \rightarrow D^0 \pi_S^+ \rightarrow \{K\pi\} \pi_S^+$ are discussed. The expected amounts are quantified using the signal and the minimum bias Monte Carlo sample. The signal sample corresponds to a high luminosity and it provides Monte Carlo truth association, i.e reconstructed particles are matched to Monte Carlo generated particles and therefore it is possible to assure that particles are correct reconstructed or to determine the background type of particles. But it does not reflect the background composition that is expected in the experiment. Especially the combinatoric backgrounds are larger in data analysis. For this reason the minimum bias sample is used to estimate these backgrounds. It corresponds to a low luminosity and it does not provide Monte Carlo truth association. Therefore a 2-dim fit to the $\Delta m - M_{D_0}$ distribution is used to estimate the number of signal and background candidates. The fit is performed in Chapter 10.

Signal and background candidates are counted only in the region of Δm and M_{D_0} which contains most of the signal. The signal region is defined as:

$\begin{aligned} 1843.8 < M(D^0) < 1885.8 \quad (3\sigma) \\ 4.45 < \Delta m < 7.27 \quad (3\sigma) \end{aligned}$
--

Table 7.1: Signal region.

The different types of background are discussed in the following.

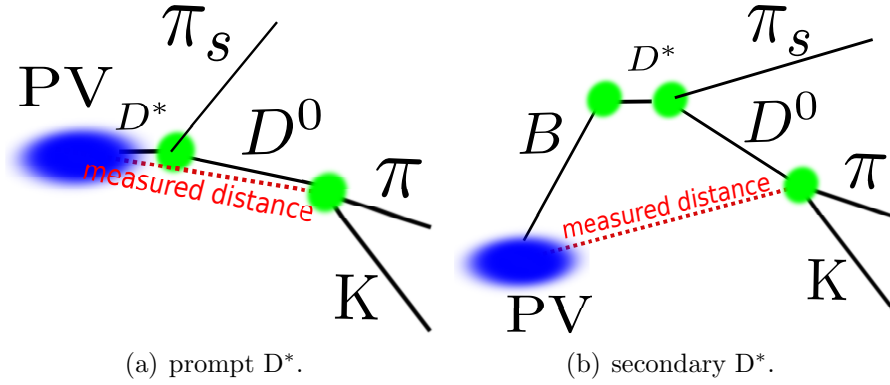


Figure 7.1: For prompt D^* 's (a) the primary vertex as production vertex of the D^0 is a good approximation. But for secondary D^* 's from B decays (b), the measured flight distance from the primary vertex is larger than the real flight distance of the D^0 .

7.1 Secondary D^* background

In this analysis prompt D^* 's are considered. Therefore, and because of the very short D^* lifetime the primary vertex can be used as decay vertex of the D^* . For prompt D^* 's the primary vertex is considered to be the origin of the D^0 and the π_S , see Figure 7.1(a).

The selection, especially the pointing variables, favour prompt D^* 's. Nevertheless after the selection a small number of D^* coming from a secondary vertex is remaining. The only known source for such secondary D^* 's are decays of B mesons. The origin of these candidates is illustrated in Figure 7.1(b). It is obvious that for these candidates the primary vertex cannot be used as production vertex and thus the measurement of the D^0 lifetime is wrong. The lifetime for background and signal candidates is shown in Figure 7.2. Background candidates have larger lifetimes than the signal. With the selection applied both distributions have a similar shape and therefore, the D^0 lifetime can not separate signal and background.

The background consists of correct reconstructed D^* 's, thus signal and secondary D^* background have the same shape in the $\Delta m - M_{D^0}$ plane. Also, in most other quantities signal and background are identical. A promising quantity to determine the number of background candidates is the D^0 impact parameter (IP). The idea is to determine the amount of secondary D^* for different lifetime

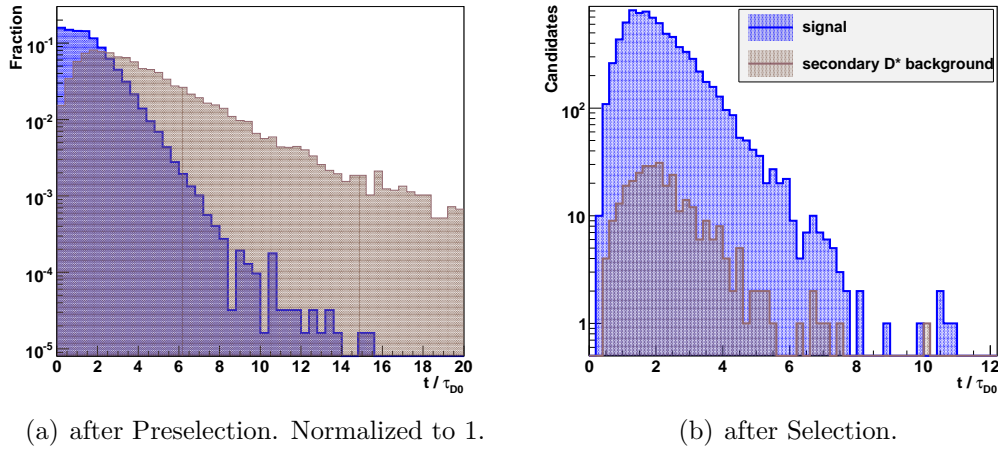


Figure 7.2: Lifetime of signal and secondary D^* background before (a) and after (b) selection. After selection the background has nearly the same lifetime as the signal. Both diagrams are normalized to 1.

bins by a fit of the D^0 impact parameter distribution. To do so the probability density functions (PDF) for prompt and secondary D^* 's have to be known. It is necessary to determine the shapes using simulated data. Figure 7.3 shows the D^0 impact parameter distribution in different bins of the D^0 lifetime. As can be seen the impact parameter distribution for the secondary D^* background is time dependent. This makes the determination of the PDF for the secondary D^* background even more prone to systematic errors.

A method for to determine the number of secondary D^* 's in data still needs to be developed. Ongoing work can be found in [29]. In the simulation, where Monte Carlo truth association can be used the number of secondary D^* background candidates over the number of signal candidates (B_{sec}/S) after the selection is measured to be $3.7 \pm 0.2\%$.

7.2 Combinatoric random π_S background

Candidates with a correct reconstructed D^0 , matched with a random π_S are one type of combinatoric background. The distribution in the $\Delta m - M_{D^0}$ plane for these candidates is shown in Figure 7.4(a). Background candidates of this type have the correct D^0 mass and therefore, their distribution is a Gaussian in M_{D^0} ,

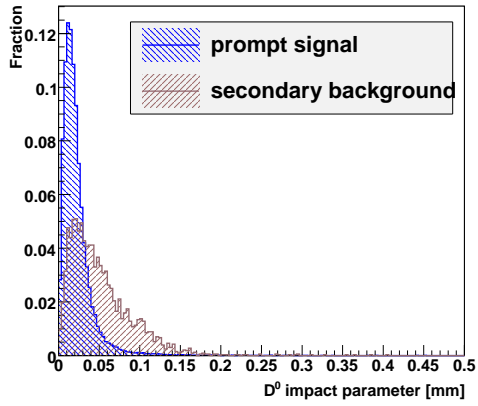
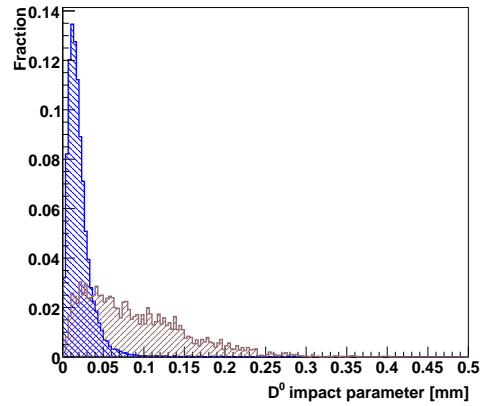
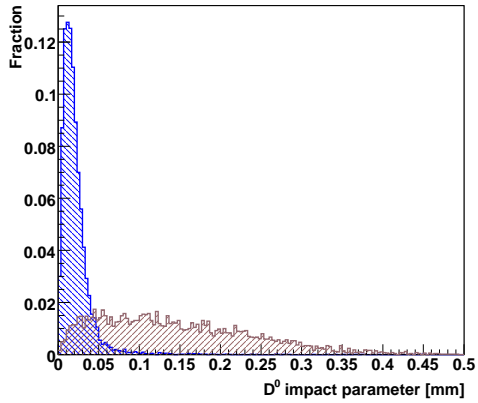
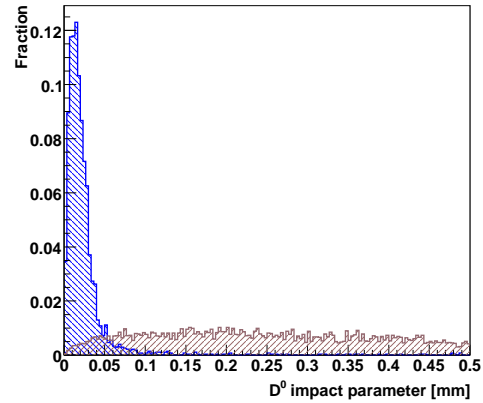
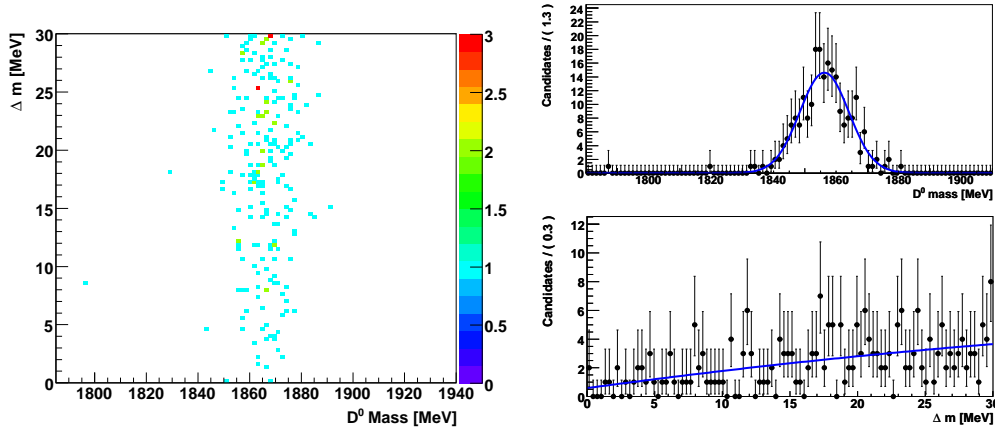
(a) D^0 lifetime between 0 and $1.5\tau_{D^0}$.(b) D^0 lifetime between $1.5\tau_{D^0}$ and $2.5\tau_{D^0}$.(c) D^0 lifetime between $2.5\tau_{D^0}$ and $4\tau_{D^0}$.(d) D^0 lifetime between $4\tau_{D^0}$ and ∞ .

Figure 7.3: D^0 impact parameter distribution for prompt signal (blue) and secondary D^* background (brown) in four different bins of the D^0 lifetime τ_{D^0} . Histograms are normalized to 1.



(a) Selected and triggered random π_S back- (b) Projections in Δm and M_{D^0} and the fitted PDF.
ground candidates.

Figure 7.4: Random π_S background.

as can be seen Figure 7.4(b). Contrary to the signal which has also a Gaussian shape in Δm the mass difference of the candidates is dispersed in Δm , because the π_S and the D^0 of the background candidates do not originate from the same D^* . The amount of random π_S background cannot be estimated from the signal Monte Carlo sample because it contains only the signal decay and more combinatoric background is expected in data. To determine the random π_S background in the minimum bias Monte Carlo sample the background shape needs to be known.

Random π_S background can be described in M_{D^0} by a double Gaussian with a shared mean and in Δm by a polynomial of 2nd order. The product of the M_{D^0} and Δm part gives an ansatz for the background pdf:

$$\begin{aligned}
 PDF_{random \pi_S}(\Delta m, M_{D^0}) = & const \times \left(1 + par_{\Delta m}^{0, \pi_S} \cdot \Delta m + par_{\Delta m}^{1, \pi_S} \cdot (\Delta m)^2 \right) \\
 & \times \left(f_{M_{D^0}}^{\pi_S} e^{-\left(\frac{M_{D^0} - \mu_{M_{D^0}}^{\pi_S}}{2\sigma_{M_{D^0}}^{1, \pi_S}} \right)^2} + (1 - f_{M_{D^0}}^{\pi_S}) e^{-\left(\frac{M_{D^0} - \mu_{M_{D^0}}^{\pi_S}}{2\sigma_{M_{D^0}}^{2, \pi_S}} \right)^2} \right)
 \end{aligned}
 \tag{7.1}$$

The PDF is fitted to background candidates from the signal sample. The projections in M_{D^0} and Δm of the data points and the fit function is shown in Figure 7.4(b). The resulting shape parameters are listed in Table 7.2. In Chapter 10 the shape parameters are fixed and the number of background candidates is determined from the fit. The result of the fit procedure in Chapter 10 for the ratio

Fit parameter	Fit value
$par_{\Delta m}^{0,\pi_S}$	2.2 ± 0.2
$par_{\Delta m}^{1,\pi_S}$	-1.473 ± 0.004
$f_{MD0}^{\pi_S}$	0.98 ± 0.01
$\mu_{MD0}^{\pi_S}$	1866.2 ± 0.5
σ_{MD0}^{1,π_S}	7.9 ± 0.4
σ_{MD0}^{2,π_S}	100 ± 75

Table 7.2: Shape parameters of random π_S background description.

of random π_S background to RS(WS) signal candidates is $B/S = 0.6\%(16\%)$.

7.3 Partially reconstructed B background

Another type of background candidates are partially reconstructed B mesons. For example, the decay $B \rightarrow D^0 \pi + X$ is reconstructed as $D^* \rightarrow D^0 \pi$. The D^0 is correctly reconstructed and the $D^0\pi_S$ combination, originating from a B, is identified as D^* . This background has the same distribution in the Δm and M_{D0} as the random π_S background. The candidates have the correct D^0 mass but in Δm the distribution is flat because the π_S is not originating from a D^* decay. Figure 7.4(b) shows the distribution of these background candidates for RS events. This background cannot be distinguished in Δm and M_{D0} from random π_S background therefore, this background is included in the number of random π_S background candidates resulting from the fit.

7.4 Combinatoric D^0 background

Combinatoric D^0 background consists of random combinations of pions and kaons. In the $\Delta m - M_{D0}$ plane, these candidates are uniformly distributed. As illustrated in Figure 7.6. After trigger and selection no combinatorial D^0 candidates are remaining in the signal sample. For the minimum bias sample one can assume that there is also no combinatorial D^0 background, see Figure 10.1. With this assumption one can expect that the number of combinatorial D^0 background candidates is smaller than 2.3 (@90% confidence level), while the number of RS(WS) signal candidates is 282(1) and therefore the ratio of background to RS(WS) signal candidates is expected to be smaller than 0.8%(23%).

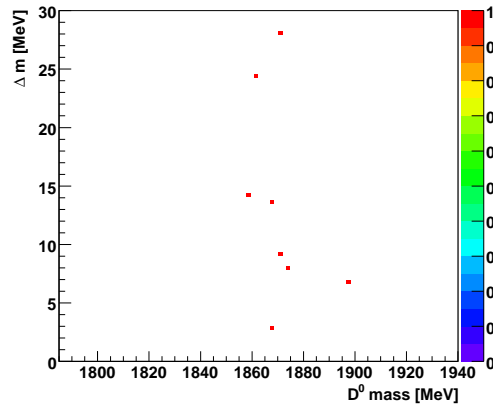


Figure 7.5: Partially reconstructed B background candidates in the $\Delta m - M_{D^0}$ plane. Shown are triggered and selected RS candidates.

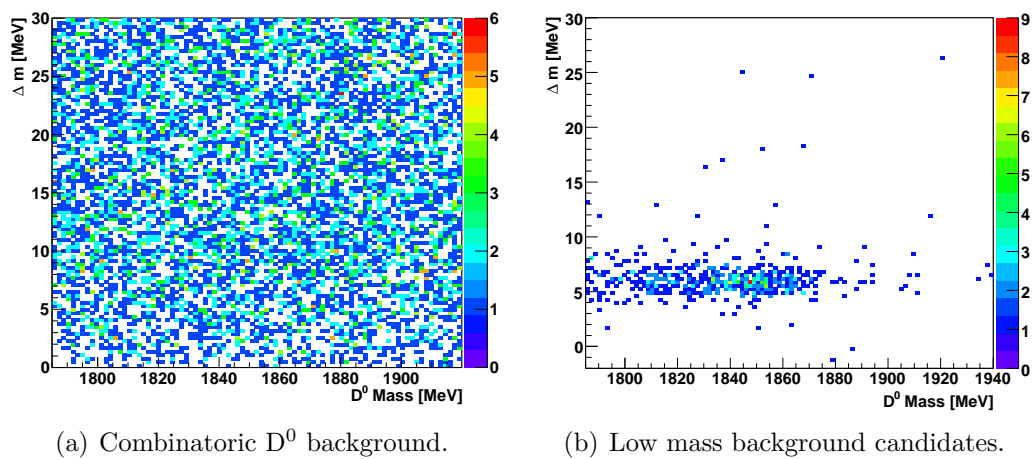


Figure 7.6: Background distributions before selection.

7.5 Low mass background

In the case of a D^0 decaying through $D^0 \rightarrow K^- \pi^+ + X$ it is possible that the 3rd daughter particle (for instance a π^0) is not reconstructed and thus the mass of the reconstructed D^0 candidate is shifted to lower values. In the subsequent reconstruction of the D^* , the D^* mass is also shifted while the mass difference Δm (see Equation 6.1) is not shifted and has values similar to correct reconstructed candidates. Figure 7.6 shows the $\Delta m - M_{D^0}$ distribution without the selection applied. The amount of this type of background is expected to be different between the signal Monte Carlo sample and the minimum bias sample because D^0 three body decays are not explicitly included in the signal sample. In order to determine the background contribution on minimum bias the background shape needs to be known. Unfortunately the statistic of the signal Monte Carlo sample is too low to determine the background shape of triggered and selected candidates. Therefore in Chapter 10 the background shape is approximated by a straight line with floating slope in M_{D^0} and a double Gaussian with the same shape as the signal in Δm .

The fit procedure gives an estimate for the ratio of misreconstructed D^0 background to RS(W) signal candidates of 1.3%(36%). Misreconstructed D^0 background refers here to all types of background with the shape described above. Without the knowledge of the background shapes low mass background cannot be separated.

7.6 Reflection background

Reflection background candidates are candidates with at least one misidentified final state particle. For instance the decay $D^0 \rightarrow K K$ can be reconstructed as $D^0 \rightarrow K \pi$, if one of the kaons is misidentified as pion. The misidentification of one D^0 daughter causes a shifted D^0 mass. The shift is of the order ± 100 MeV, as can be seen in Figure 7.7. More background candidates have values below the D^0 mass because a misidentification of a kaon as pion is more likely than the other way. According to the explanations for the low mass background, the Δm distribution is similar to the signal. Also for this background the determination of the background shape is not possible due to limited statistics. It can be expected that the absolute number of background candidates are the same

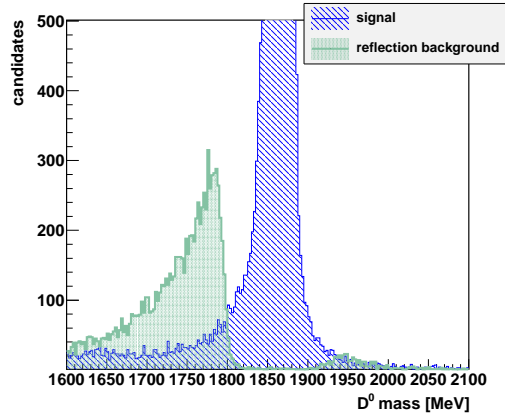


Figure 7.7: Signal candidates (blue) and candidates with one misidentified D^0 daughter particle (turquoise). In order to illustrate the distribution a wide mass window was chosen. For background candidates at low mass a kaon was misidentified as pion and for high masses a pion was identified as kaon.

for WS and RS. The analysis of the signal Monte Carlo sample shows that the number of background events in the signal region is smaller than 3.89 candidates (90% confidence level) compared to 47 selected WS signal candidates. Therefore the number of background candidates over number of WS signal candidates can be expected to be smaller than 8.3%.

Double misidentification background

It is also possible that both D^0 daughters are misidentified. That means the pion is identified as kaon and vice versa. So a $D^0 \rightarrow K^- \pi^+$ is reconstructed as $D^0 \rightarrow \pi^- K^+$ and thus a RS event is reconstructed as WS event. The shape of signal and background are the same and without particle identification this background contribution is much larger than the WS signal itself. In the signal Monte Carlo data sample 47 WS signal candidates and one double misidentified background candidate remains. Therefore, the background can be expected to be smaller than 3.89 candidates (90% confidence level) within the statistic used. The number of background candidates over number of signal candidates is therefore expected to be smaller than 8.3%. Even though this background is large in the CDF analysis [2] LHCb benefits from a good particle identification.

Chapter 8

Trigger

In this chapter the trigger efficiencies for the selection described in Chapter 6 is evaluated and the lifetime dependent trigger acceptance is studied. The simulated trigger efficiencies in this chapter, and all other diagrams of L0 and HLT1 triggered events in this thesis, use a trigger setting¹, which is optimized for nominal luminosity. The total output bandwidth of the trigger is limited by the storage hardware, and the output rate of a trigger line is determined by its threshold settings. The trigger scenario discussed here is a set of thresholds which favour the selection of charm events.

8.1 Trigger efficiencies and trigger lines

The following trigger efficiencies for the L0 hardware trigger are given with respect to the number of events with at least one reconstructed and selected $D^{*+} \rightarrow D^0(K\pi)\pi_S^+$ candidate:

$$\epsilon_{eff,L0} = \frac{\# \text{ (selected \& L0 triggered events)}}{\# \text{ (selected events)}} \quad (8.1)$$

Because of this definition the trigger efficiencies are only valid for the selection shown used here. The efficiencies for the different L0 trigger lines are listed in Table 8.1. The table shows that most of the signal is triggered by the hadron lines. A total trigger efficiency for the L0 trigger of $64.8 \pm 0.16\%$ is expected.

In the first stage of the HLT (HLT1) also the different hadron lines are the

¹The exact description of the trigger scenario is Physics_10000Vis_1000L0_40Hlt1_CharmingHlt2_Jul09.

Level 0 stream	signal selection efficiency /%
Hadron lines	58.2 ± 1.5
Electron line	11.6 ± 0.7
Muon line	7.8 ± 0.6
Photon lines	2.5 ± 0.3
Di-muon line	1.4 ± 0.2
Total	64.8 ± 0.16

Table 8.1: L0 trigger efficiencies of the different trigger lines. The efficiencies are calculated with respect to offline selected events.

most efficient, as shown in Table 8.2. The efficiencies are given with respect to the number of L0 triggered events with at least one selected signal candidate:

$$\epsilon_{eff,HLT1} = \frac{\# \text{ (selected \& L0} \times \text{HLT1 triggered events)}}{\# \text{ (selected \& L0 triggered events)}} \quad (8.2)$$

The overall HLT1 trigger efficiency is $47.91 \pm 0.02\%$. This results in a combined trigger efficiency for L0 and HLT1 of $31.1 \pm 1.1\%$.

A detailed analysis revealed that a large amount of events which have been triggered are selected because of particles belonging to the signal decay. Only a fraction of $(6.1 \pm 0.3)\%$ events are triggered by a particle which does not belong to the signal decay and thus are triggered independent of signal.

HLT1 trigger stream	signal selection efficiency /%
Di-hadron	33.76 ± 0.01
Single hadron	27.8 ± 0.013
Electron+track	1.54 ± 0.31
Single electron	2.71 ± 0.41
μ +track	1.0 ± 0.3
\sum single- μ	16.42 ± 0.35
\sum di- μ	1.5 ± 0.3
\sum others	< 1
Total	47.91 ± 0.02

Table 8.2: HLT1 trigger efficiencies with respect to offline selected and L0 triggered events.

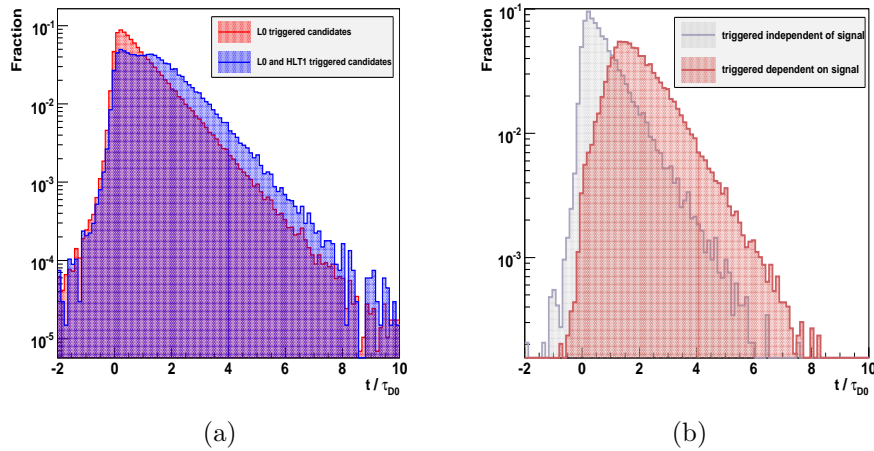


Figure 8.1: (a) D^0 lifetime distributions for L0 triggered and for L0 \times HLT1 triggered candidates. (b) D^0 lifetime distributions for events triggered independent of signal and triggered dependent on signal. The candidates in these diagrams were selected by the preselection. All diagrams are normalized to 1.

8.2 D^0 lifetime dependent acceptance

The D^0 lifetime is correlated with a large number of quantities. In Chapter 6.5 the effect of the selection on the D^0 lifetime distribution is shown. The trigger algorithms select events on the basis of quantities which are correlated to the D^0 lifetime. Therefore the D^0 lifetime distribution is influenced. Influenced means that the trigger efficiency is dependent on the D^0 lifetime. For instance the fraction of triggered candidates with low lifetimes is smaller than for candidates with large lifetime. Here the results of a Monte Carlo study are presented.

The L0 trigger selects events on the basis of momenta and transverse energy deposition in the calorimeter. It does not use track parameters because at this stage no track estimates are available. Momenta and transverse energy deposition are quantities that are not correlated with the D^0 lifetime and an exponential distribution is expected for L0 triggered events. The red shaded diagram in Figure 8.1(a) shows the D^0 lifetime distribution for L0 triggered events and it can be seen that it is an exponential except small deviations at small lifetimes due to lifetime resolution.

The HLT1 algorithms are partly based on quantities which are correlated with the D^0 lifetime. At this stage of the trigger a better track estimate is

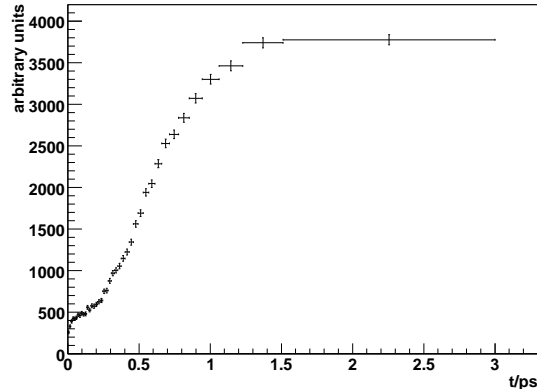


Figure 8.2: D^0 lifetime distribution with an exponential increasing bin width. An undistorted D^0 lifetime distribution would be indicated by a constant line. The D^0 lifetime distribution is distorted up to approximately 1.2 ps.

available and track parameter can additionally be used for event selection. Most of the signal is triggered by the HLT1 hadron lines and these lines use the impact parameter for event selection. The D^0 lifetime distribution for HLT1 triggered D^0 candidates is shown in Figure 8.1(a). Apparently the lifetime distribution has not of exponential shape for lifetimes smaller $2\tau_{D^0}$. The distribution shows that candidates with low lifetime are selected with a different efficiency. This bias must be taken into consideration in a D^0 lifetime measurement. As explained in Chapter 4.1 this bias does not change the values of the mixing parameter determined by the ratio method because it is applied to RS and WS in the same way. Nevertheless the number of data at low lifetimes is lowered and this will influence the errors of the mixing parameters, see Chapter 11. Furthermore it is possible to collect a sample without the trigger bias by using only events triggered independent of the signal decay particles. This means that the trigger is deployed by a particle which does not belong to the signal decay, but for instance by a particle from the second c -quark in the $c\bar{c}$ -event. A distribution for these events is shown in Figure 8.1(b).

The D^0 lifetime dependent acceptance of the L0 and HLT1 trigger is shown in Figure 8.2. The bin width in the diagram increases exponentially (with the D^0 lifetime $\tau_{D^0} = 0.410$ ps as scale). A D^0 lifetime distribution with an exponential shape results in a constant line. The figure shows that the D^0 lifetime distribution is distorted up to approximately 1.2 ps.

Chapter 9

D⁰ lifetime and lifetime resolution

In this chapter the resolution of the D⁰ decay and production vertices and the D⁰ lifetime resolution is shown and discussed. In the last part the D⁰ lifetime acceptance of the trigger and the selection is presented.

In Figure 9.1 the D⁰ lifetime distribution for triggered and selected events is shown. The Monte Carlo sample used in the diagram, corresponds to an integrated luminosity of 16 nb^{-1} . A comparable data set can be collected within a couple of seconds.

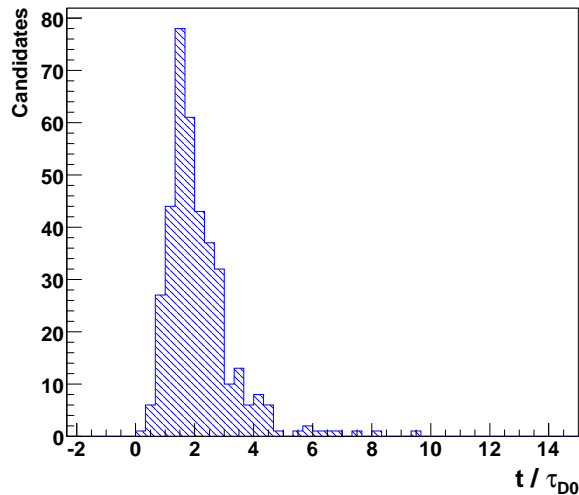


Figure 9.1: D⁰ lifetime distribution of triggered and selected candidates from the minimum bias Monte Carlo sample.

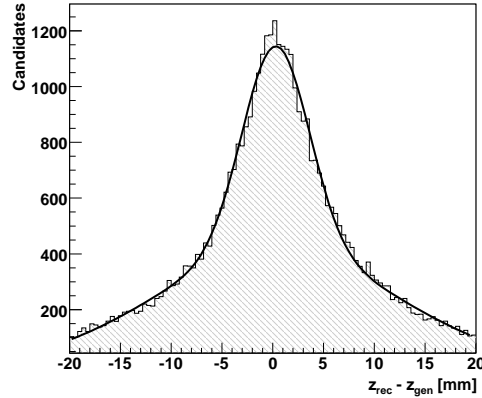


Figure 9.2: Vertex resolution for z component of D^* decay vertex. A fit of function 9.3 gives a core resolution of $\sigma_Z = (3.28 \pm 0.07)$ mm for the inner part.

resolution in μm	D^0 vertex	D^* vertex	primary vertex
σ_x	24	234	6.4
σ_y	20	174	6.5
σ_z	325	3282	31
$\sigma_{\tau_{D0}}$	—	$(370 \pm 5) fs$	$(30.7 \pm 0.4) fs$

Table 9.1: Resolutions of D^0 , D^* , and primary vertex in the directions x , y and z . The D^* vertex resolution in z -direction is a multiple of the mean D^0 flight length. In the last row lifetime resolutions for different production vertices are given. The first uses the D^* decay vertex as D^0 production vertex and the second one uses the primary vertex.

9.1 Vertex and D^0 lifetime resolution

The D^0 lifetime τ_{rec} is determined from the measured distance (D) between production and decay vertex and the D^0 momentum:

$$\tau_{rec} = \frac{D}{c\beta\gamma} \quad (9.1)$$

With the Lorentz factor γ and the velocity in terms of the speed of light β . The average D^0 lifetime is $\tau_{D0} = (410.1 \pm 1.5)10^{-15}s$ [28] and selected D^0 candidates have a mean γ of 41 and therefore the mean flight distance (\bar{D}) in the lab frame can be estimated by:

$$\bar{D}_{lab} = \tau_{D0} c\beta\gamma \approx 5mm \quad (9.2)$$

The time resolution is basically given by the resolution of production and decay vertex. In the further analysis the primary vertex is used as D* decay vertex. In Figure 9.2 the difference between reconstructed value and true value of the z-component of the D* vertex is shown. A fit of the sum of two gauss functions with the same mean value but different width, determines the vertex resolution:

$$res(t) = \frac{N}{\sqrt{2\pi}} \left(\frac{f}{|\sigma_1|} \exp\left(-\frac{(t-\mu)^2}{2\sigma_1^2}\right) + \frac{1-f}{|\sigma_2|} \exp\left(-\frac{(t-\mu)^2}{2\sigma_2^2}\right) \right) \quad (9.3)$$

The core resolutions of D* and D⁰ vertices are listed in Table 9.1. It can be seen that especially the z-resolution of the D* vertex is of the order of the D⁰ mean flight length. The worse D* vertex resolution is caused by a small opening angle of the D* daughter particles D⁰ and π_S. Therefore, using prompt D*'s has a clear advantage because of the well determined primary vertex.

The D⁰ lifetime resolution is determined according to the vertex resolution by the difference between measured and true lifetime as shown in Figure 9.3. A fit of Equation 9.3 to the distribution determines a core resolution of (30.7 ± 0.4) fs. The effective resolution of a double gauss is:

$$\sigma_{tot} = \sqrt{f \sigma_1^2 + (1-f) \sigma_2^2} \quad (9.4)$$

This gives an effective resolution of 47 fs for the D⁰ lifetime.

In case of using the reconstructed D* vertex instead of the primary vertex as production vertex of the D⁰ the resolution of the core Gaussian increases to (370 ± 5) fs. Contrary to the analysis described here, it is also possible to use D* from B decays for the mixing measurement. In this case the lifetime resolution is a priori quite bad, as shown. In [30] an attempt was made to improve the D* vertex resolution from B decays by using another charged track from the B decay chain. A D⁰ lifetime resolution of the same order of magnitude as for prompt D*'s was found.

9.2 D⁰ lifetime acceptance

As shown in Chapter 6.5 and 8.2 the acceptance of trigger and selection depends on the D⁰ lifetime. Therefore, the time dependent acceptance of trigger and se-

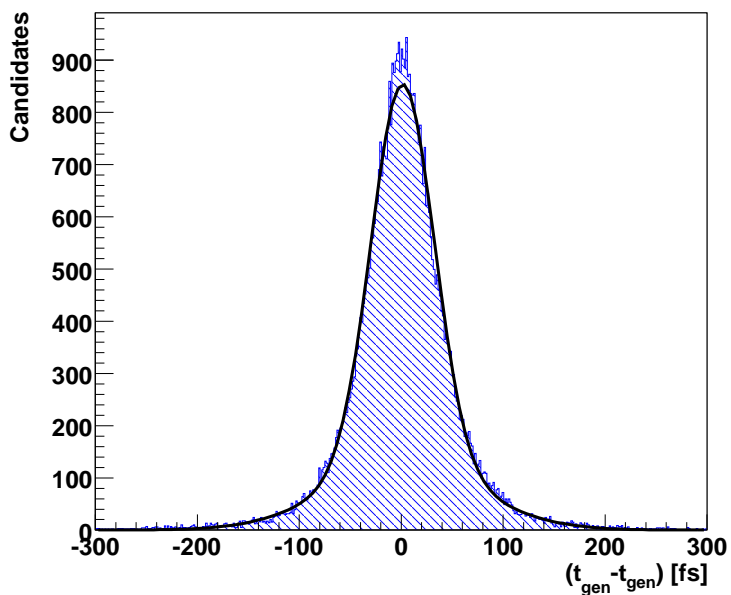


Figure 9.3: D^0 lifetime resolution. A fit of a double gauss function (Eqn. 9.3) gives a core resolution of 30.7 ± 0.4 fs.

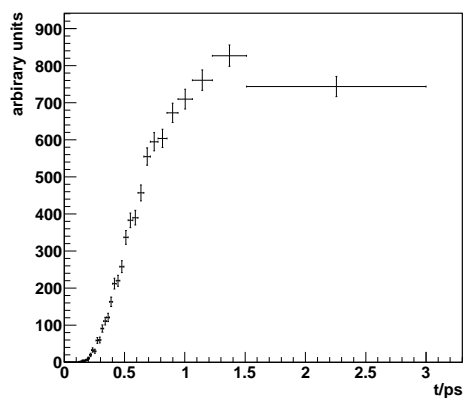


Figure 9.4: D^0 lifetime dependent acceptance for triggered and selected candidates. The acceptance is lowered up to approximately 1.2 ps.

lection needs to be known. According to Figure 6.18 and 8.2, Figure 9.4 shows the D^0 lifetime distribution of selected and triggered events in bins with exponentially increasing width. The Figure shows that trigger and selection influence the D^0 lifetime distribution up to approximately 1.2 ps. For lifetimes above 1.2 ps the figure shows that the acceptance is flat.

Chapter 10

Signal yield

This chapter describes the estimation of the expected number of signal and background candidates using the minimum bias Monte Carlo data sample. With this result the expected level of background and the expected number of signal candidates per integrated luminosity is given.

The minimum bias sample does not provide Monte Carlo truth association, i.e. reconstructed particles are not matched to Monte Carlo generated particles and therefore it is not possible to assure that particles are correct reconstructed or to determine the background type of particles. This sample is close to the conditions of real data analysis.

Selected and triggered candidates are shown in Figure 10.1. The signal yield is determined in a two dimensional fit to the $\Delta m - M_{D^0}$ distribution. The probability density functions (PDF) for signal and background description are discussed in the following.

As background contributions combinatoric background from random π_S and misreconstructed D^0 background are considered. Misreconstructed D^0 background is here a generic term which describes backgrounds with a distribution similar to the signal in Δm but different in M_{D^0} . These backgrounds essentially are low mass (Section 7.5) and reflection background (Section 7.6). Combinatoric D^0 background is not included in the background description because from Figure 10.1 the number of D^0 background candidates after the selection can be estimated to be zero in this sample.

The shape parameters of signal and backgrounds have to be determined in the signal Monte Carlo sample because this sample provides Monte Carlo truth

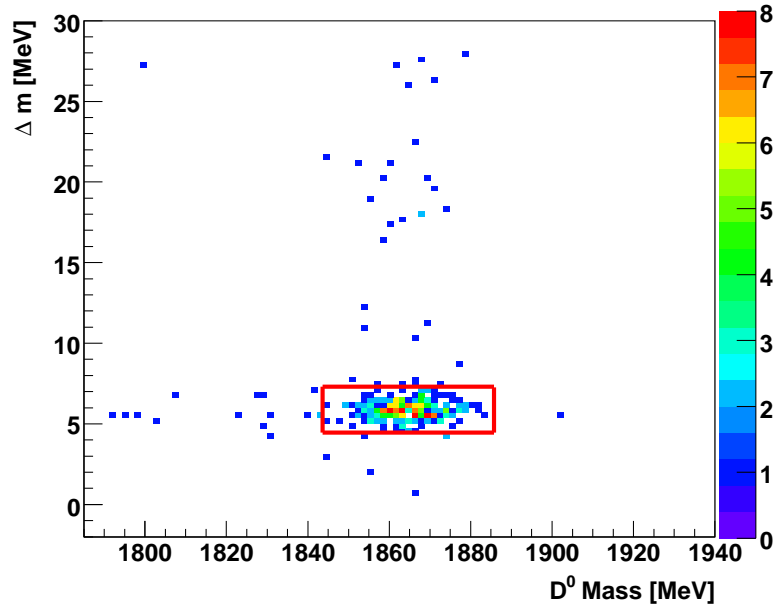


Figure 10.1: Candidates after selection in the $\Delta m - M_{D^0}$ plane. The signal region (defined in Table 7.1) is highlighted.

association. For the determination of the shapes selected and triggered candidates are used. Unfortunately, the statistic of the signal sample is too low to determine the shape of the misreconstructed D^0 backgrounds and therefore not all shape parameters can be fixed in the fit procedure.

For creating the PDF's and fitting the PDF's to the Monte Carlo data sample the *ROOT* [31] environment and the *rooFit* [32] library for advanced data modelling are used. *rooFit* automatically calculates the normalization constants.

Fit parameter	Fit value
f_{MD0}	0.949 ± 0.005
μ_{MD0}	1864.7 ± 0.08
σ_{MD0}^1	6.9 ± 0.07
σ_{MD0}^2	35.111 ± 3.13
$f_{\Delta m}$	0.83 ± 0.02
$\mu_{\Delta m}$	5.881 ± 0.006
$\sigma_{\Delta m}^1$	0.48 ± 0.01
$\sigma_{\Delta m}^2$	1.19 ± 0.05

Table 10.1: Shape parameter of the signal PDF.

10.1 Signal probability density function

The ansatz for the signal PDF is the product of double Gaussian distributions in Δm and M_{D0} . Both double Gaussians have a common mean:

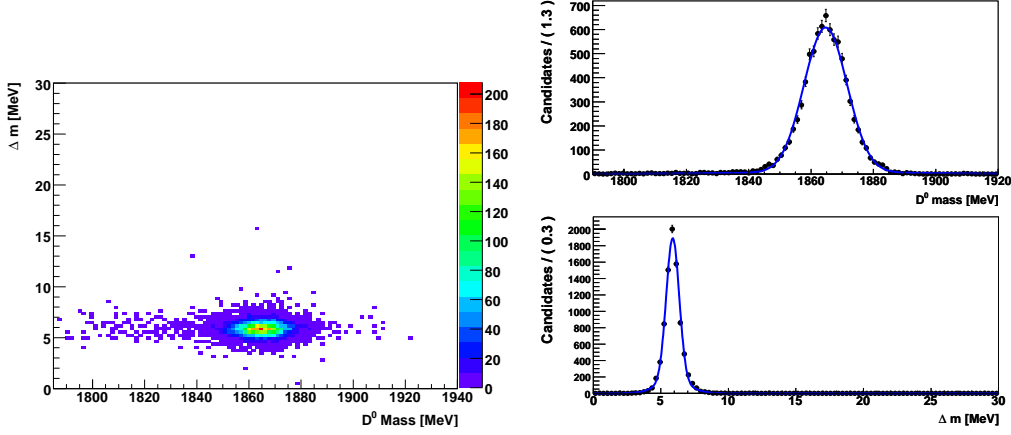
$$\begin{aligned}
 PDF_{signal}(\Delta m, M_{D0}) = const \times & \left(f_{\Delta m}^{sig} e^{-\left(\frac{\Delta m - \mu_{\Delta m}^{sig}}{2\sigma_{\Delta m}^{sig}}\right)^2} + (1 - f_{\Delta m}^{sig}) e^{-\left(\frac{\Delta m - \mu_{\Delta m}^{sig}}{2\sigma_{\Delta m}^{sig}}\right)^2} \right) \\
 & \times \left(f_{MD0}^{sig} e^{-\left(\frac{M_{D0} - \mu_{MD0}^{sig}}{2\sigma_{MD0}^{sig}}\right)^2} + (1 - f_{MD0}^{sig}) e^{-\left(\frac{M_{D0} - \mu_{MD0}^{sig}}{2\sigma_{MD0}^{sig}}\right)^2} \right)
 \end{aligned} \tag{10.1}$$

The function is fitted by an unbinned maximum likelihood fit to Monte Carlo data from the signal sample. The fit result is shown in Figure 10.2(b) and the fit parameter are summarized in Table 10.1.

10.2 Background probability density functions

The PDF for the random π_S background is determined in Chapter 7.2. The fit result is shown in Figure 7.4 and the results for the shape parameters are listed in Table 7.2. In the number of random π_S background candidates, the background from partially reconstructed B mesons (see Chapter 7.2) is included because both background classes have the same shape in Δm and M_{D0} . The contribution is expected to be small and thus here is only referred to random π_S background.

Misreconstructed D^0 candidates have a shifted D^0 mass but the Δm distribution is similar to the signal. As explained before, it is not possible to determine the shape from the signal sample and therefore a very simple ansatz is chosen. It



(a) Signal candidates in $\Delta m - M_{D^0}$ plane. (b) Projections in Δm and M_{D^0} and fit function.

Figure 10.2: Candidates from signal Monte Carlo sample. The shape of the signal distribution is determined by a fit of Equation 10.1.

consists of a double Gaussian in Δm with the shape parameters from the signal distribution multiplied with a polynomial of 1st order in M_{D^0} :

$$\begin{aligned}
 PDF_{misrecD^0}(\Delta m, M_{D^0}) = & const \times \left(f_{\Delta m}^{sig} e^{-\left(\frac{\Delta m - \mu_{\Delta m}^{sig}}{2\sigma_{\Delta m}^{1,sig}}\right)^2} + (1 - f_{\Delta m}^{sig}) e^{-\left(\frac{\Delta m - \mu_{\Delta m}^{sig}}{2\sigma_{\Delta m}^{2,sig}}\right)^2} \right) \\
 & \times \left(1 + slope_{MD^0}^{misrecD^0} \cdot M_{D^0} \right)
 \end{aligned}
 \tag{10.2}$$

The only floating shape parameter is the slope of the polynomial in M_{D^0} . It is determined later in the fit.

10.3 Fit results

Using the PDF's with the shape parameters as previously extracted the yield of signal and background in the minimum bias data sample is determined by an extended unbinned maximum likelihood fit. The fit results are summarized in Table 10.2. The projections of the data points and the fitted PDF on M_{D^0} and Δm are shown in Figure 10.3(a) and (b). The residuals of the fitted function and the data in the lower part of Figure 10.3 indicate the good quality of the fit.

The good description of the fit indicates that the shape of signal and back-

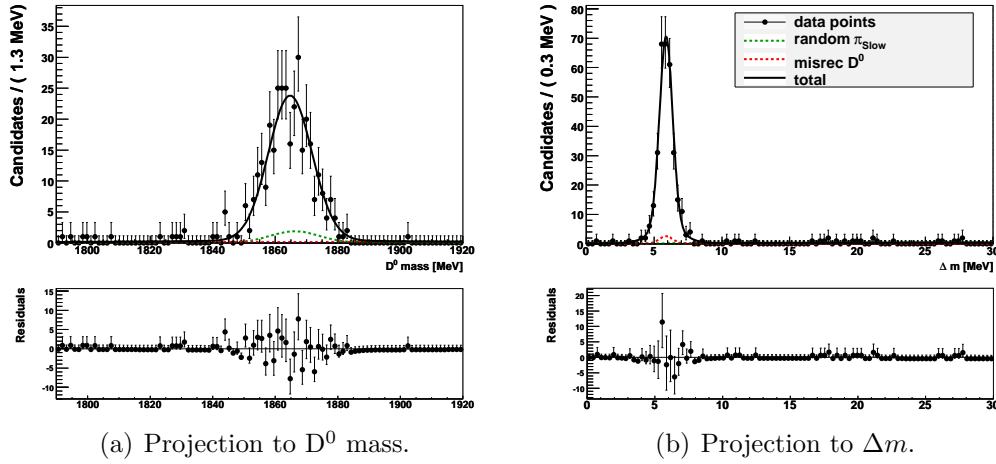


Figure 10.3: Projections of data points and PDF to D^0 mass and Δm . Below the residuals between the fitted function and the data points is shown.

Floating Parameter	Fit value
signal candidates	303 ± 18
random π_S candidates	28.8 ± 5.7
misreconstructed D^0 candidates	11.6 ± 5.6
$\text{slope}_{MD^0}^{\text{misrec}D^0}$	28.5 ± 8.5

Table 10.2: Results of the extended unbinned maximum likelihood fit to the minimum bias data sample.

grounds determined earlier match the backgrounds on the minimum bias sample. Table 10.3 shows the correlations of the fit parameters. It can be seen that the correlation between the shape parameter of the misreconstructed D^0 background and the other fit parameters is small.

Signal and background candidates are counted all over the $\Delta m - M_{D^0}$ plane in this listing. The fraction of signal and background within the signal region (see Figure 10.1) can be calculated and is given in Table 10.4. The number of signal candidates still contains secondary D^* background candidates. The ratio of signal over background (S/B) is measured to be 54 ± 18 for RS events. For WS events the ratio is 0.19 ± 0.07 . It is assumed that the types of background, considered here, are constant in their absolute value for RS and WS. This is true for the random π_S background but for misreconstructed D^0 background it is an approximation and further studies are needed. The number of WS signal candidates is the number of

	$\text{slope}_{MD0}^{\text{misrec}D^0}$	misrec. D^0 cand.	random π_S cand.	signal cand.
$\text{slope}_{MD0}^{\text{misrec}D^0}$	1	0.01	-0.012	0.004
misrec. D^0 cand.	0.01	1	-0.1	-0.148
random π_S cand.	-0.012	-0.1	1	0.014
signal cand.	0.004	-0.148	0.014	1

Table 10.3: Correlations of the fit parameters.

	RS candidates	WS candidates (scaled)
signal	282 ± 17	1 ± 0.07
random π_S	1.6 ± 0.3	1.6 ± 0.3
misreconstructed D^0	3.6 ± 1.7	3.6 ± 1.7
S/B	54 ± 18	0.19 ± 0.07

Table 10.4: Estimated number of signal and background candidates after selection in the signal region in the minimum bias sample.

RS candidates scaled by the ratio between cabibbo favoured and doubly cabibbo suppressed decays $R_{WS} = 3.53_{\pm 0.08(\text{stat})}^{\pm 0.04(\text{sys})} \times 10^{-3}$. The value of R_{WS} used here was measured by BaBar [1].

Another study at LHCb on D^0 - \bar{D}^0 mixing in the decay $D^0 \rightarrow K\pi$ [30] was performed using secondary D^* 's from B decays. In this study, a 90% confidence level of $0.19 < S/B < 0.91$ with a central value of 0.39 was achieved. This is consistent with this study. The advantage of using prompt D^* 's is the much larger production rate.

In order to perform a mixing measurement the signal yield of RS and WS events has to be measured in bins of the D^0 lifetime (see Section 4). Due to lack of statistics this can not be performed on the minimum bias sample. The results derived here are input to a simplified Monte Carlo simulation which is used to study the extraction of the mixing parameters, see Chapter 11.

10.4 Alternative method of the signal yield determination

In this section an alternative method, to the method described above for the determination of the signal yield is described. Because of limited statistics this method cannot be performed.

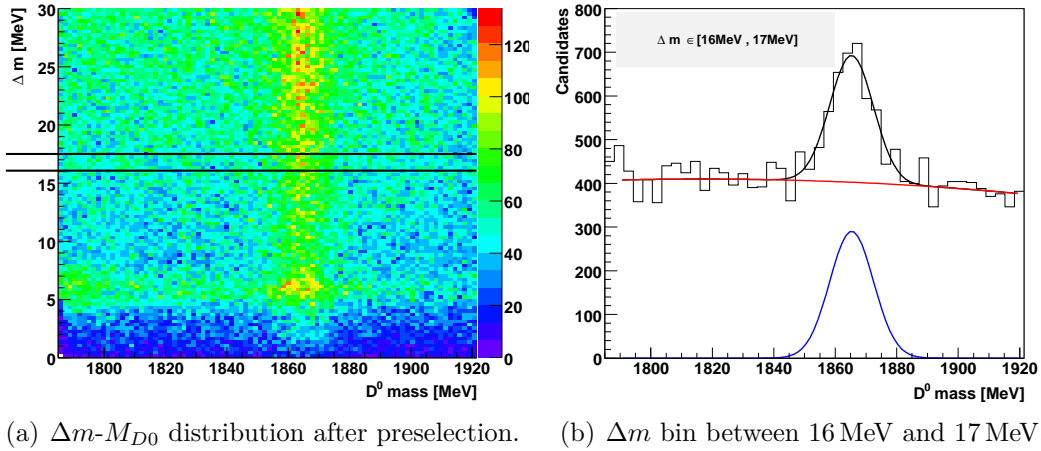


Figure 10.4: Alternative determination of signal yield by fitting the M_{D0} distributions in bins of Δm . (b) Bin Δm_i with a preliminary fit. Distribution after preselection.

The signal yield is determined by fitting the D^0 mass distribution in bins of Δm . In order to illustrate the method Figure 10.4(a) shows the $\Delta m - M_{D0}$ distribution after preselection and the M_{D0} distribution of one Δm bin (Figure 10.4(b)). In each bin Δm_i a Gaussian for the signal and a polynomial for the background is fitted in order to determine the number N_i of correct reconstructed D^0 's. The number of correct reconstructed D^* candidates can now be determined by a fit of the distribution of N_i versus Δm .

The advantage of this method is that the background dependence on Δm does not need to be known. The shape parameters for signal and background can be determined in every bin Δm_i and therefore the dependence on Δm of the shape parameters does not need to be known.

It is not yet studied if this method developed in the charm mixing analysis of CDF [2] gives better results than the method described before.

10.5 Expected signal yield

It was shown that 282 ± 17 candidates from the minimum bias sample were triggered and selected. The sample corresponds to an integrated luminosity of 16pb^{-1} , see Chapter 5.2. Therefore, the estimated signal yield per pb^{-1} is 17.6×10^3

experiment	RS($\times 10^6$)	WS($\times 10^3$)
LHCb($100pb^{-1}$)	1.8	6.25(scaled)
CDF [2]	3.0	12.7
BaBar [1]	1.1	4

Table 10.5: Comparison of signal samples.

RS candidates. The integrated luminosity for one nominal year (10^7 s) of LHCb running is $2 fb^{-1}$ and therefore $100 pb^{-1}$ corresponds to approximately 139 hours. Table 10.5 compares the expected number of signal candidates for an integrated luminosity of $100pb^{-1}$ with the datasets of CDF and BaBar. It shows that the statistics of former analysis can be collected within some weeks of data taking at nominal conditions.

Chapter 11

Extraction of the mixing parameters

In this chapter the influence of a D^0 lifetime cut and the lifetime acceptance due to trigger, selection and the contribution of background to the errors of the mixing parameters is studied using a simplified Monte Carlo simulation (Toy Monte Carlo) [33].

In a first step WS and RS decay time distributions are generated using a 'hit and miss' method. The RS decay time function is simply an exponential. For WS events a mixing model according to Equation 4.3 is considered. The D^0 lifetime resolution is realized by a gaussian model with the parameters measured in Section 9.1. The generated decay time distributions are shown in Figure 11.1(a).

The generated time distributions are analyzed by using the 'ratio' method described in Chapter 4. The WS and RS distributions are divided in bins Δt_i and the ratio $R(\Delta t_i) = \#WS/\#RS$ is evaluated. The mixing parameters are extracted by a fit of:

$$R(t) = R_{DCS} + \sqrt{R_{DCS}} \cdot y' \cdot t + \frac{x'^2 + y'^2}{4} \cdot t^2 \quad (11.1)$$

to the simulated data points. Figure 11.1(b) shows the fit (black curve) and the simulated data points. The blue curve shows the model which was used as input. The input mixing parameters are summarized in Table 11.1.

All diagrams shown here were generated using 1.3×10^6 RS events and the corresponding number of WS events. According to Section 10.5 this number of

Parameter	Value
$\sqrt{R_{DCS}}$	0.0548
y	0.01
x^2	0.0001
τ_{D0}	$410.1 fs$
$\sigma_{\tau_{D0}}$	$46.96 fs$

Table 11.1: Input parameters used in the Toy Monte Carlo simulation. D^0 lifetime from [28].

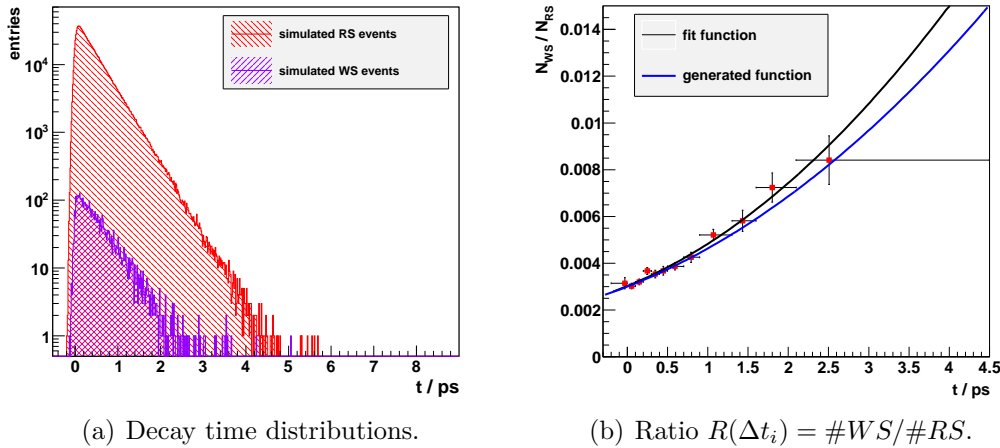


Figure 11.1: Results of toy Monte Carlo simulation. (a) Simulated decay time distributions for WS and RS events. (b) Simulated data points $R(\Delta t_i) = \#WS/\#RS$ and function $R(t)$ with fitted mixing parameters (black) and with generated parameters (blue).

events corresponds to an integrated luminosity of $72 pb^{-1}$.

To assure that the fit result has no systematic bias so-called pull distributions are shown. These show the distribution of the difference between the fitted parameter and the generated value divided by the fit error of this parameter for a large number of toy experiments. For a correct fit procedure with a correct error estimate the distribution is a gaussian with a mean value of zero and a width of one. For the pull distributions 1000 toy experiments each with 1.3×10^6 RS events were generated. The pull distributions do not show a bias or an incorrect error estimate.

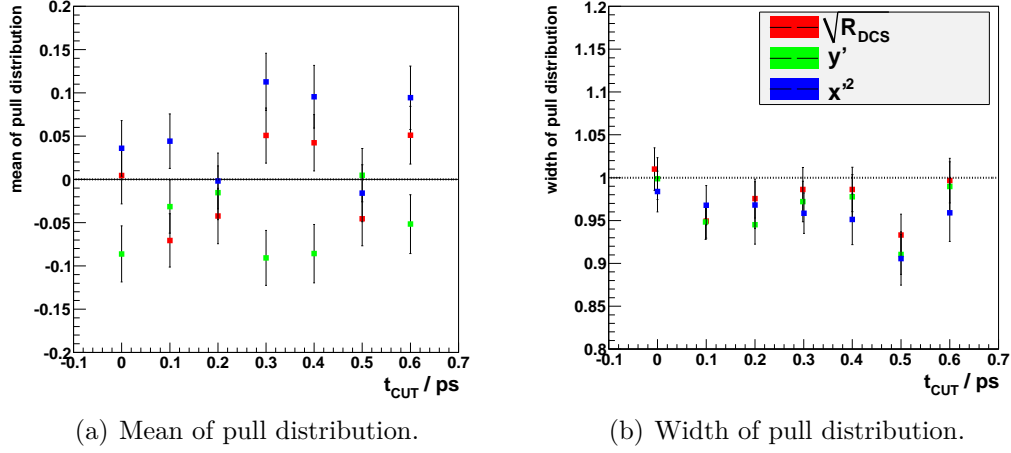


Figure 11.2: Mean and width of the pull distributions of 1000 Toy experiments for various time cuts. Mean and width were determined by a Gaussian fit to the pull distribution.

11.1 Influence of D^0 lifetime acceptance

The selection and the trigger influence the D^0 lifetime measurement. The combined effect of both is shown in Figure 9.4. Here, it is studied how the removal of all candidates with lifetimes smaller than a certain value t_{CUT} influences the measurement of the mixing parameters. The mean errors of the mixing parameters and R_{DCS} for seven different values of t_{CUT} can be seen in Figure 11.3. The values without a lifetime cut are indicated by the blue line. The errors are the RMS¹ of the error distribution of the single experiments. The errors of the mixing parameters x'^2 and y' raise moderate. The error of R_{DCS} raises rapidly with increasing values for t_{CUT} . This is plausible because R_{DCS} is the value of $R(t)$ at $t=0$ and removing all measurements at low lifetimes causes that the fit procedure loses the handle on this variable. Nevertheless, the pull distributions are not shifted or broadened significantly, as shown in Figure 11.2.

To study the effect of the lifetime acceptance due to trigger and selection an acceptance function is needed. The shape of the lifetime acceptance is approximated by the function, see Chapter 9:

$$f_{accept}(t) = a_o - \{a_1 \cdot t \cdot e^{-a_2 t - a_3} + a_4 \cdot e^{-a_5 t - a_3}\}^2 \quad (11.2)$$

¹The Root Mean Square of a set of n values is defined as: $x_{RMS} = \sqrt{\sum_{i=0}^n x_i^2 / n}$.

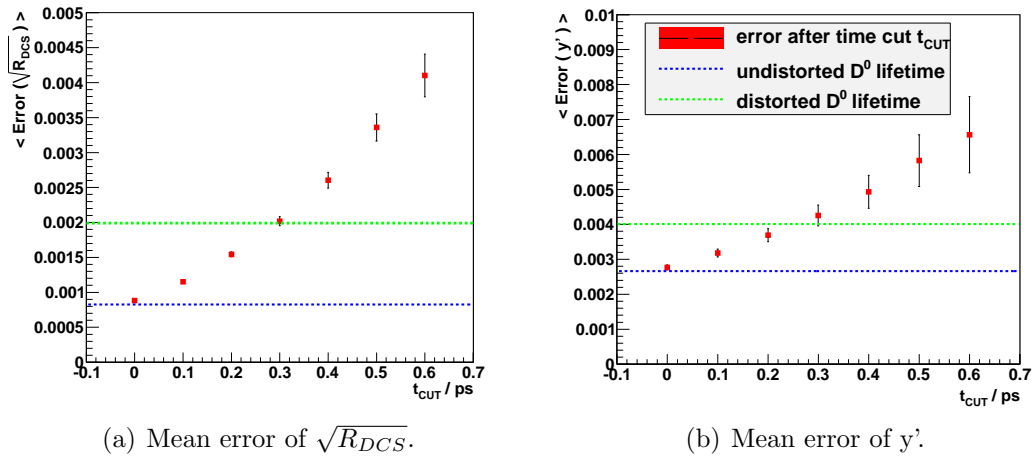


Figure 11.3: Mean errors of mixing parameters after certain time cuts. The blue dashed line indicates the errors without bias in the D^0 decay time and the green dashed line shows the influence of trigger and selection on the errors. The errors in the diagrams are the RMS of the error distributions. The mean errors are calculated from 1000 Toy experiments.

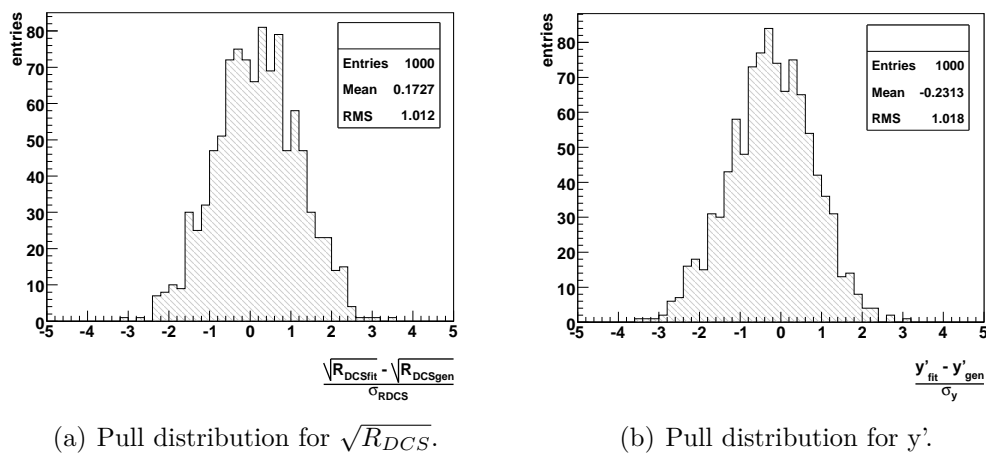


Figure 11.4: Pull distributions of the fit variables after the acceptance function was applied to the decay time distribution.

The parameters a_i are determined in order to describe the diagram in Figure 9.4.

The simulation shows that after the acceptance function was applied on the decay time distributions of WS and RS events the errors on the mixing parameters and R_{DCS} increase by a small amount. The errors are indicated by the green line in Figure 11.3. The pull distributions for the fit variables, as shown in Figure 11.4(b), are not significantly shifted or broadened. A lifetime dependent acceptance due to trigger and selection does not bias the measurement of the mixing parameters.

Fit parameter	Fit errors
R_{DCS}	0.007
y'	0.013
x^2	0.0007

Table 11.2: Error of the fit parameters with simulated background contribution.

11.2 Influence of background contribution

Up to now only the statistical errors of the signal which is the square root of the number of signal events per time bin is considered. But the background is an additional the uncertainty. A rough estimate about the background contribution to the errors is shown in the Section. In Chapter 10 the amount of random π_S and misreconstructed D^0 background was determined by a two dimensional fit in Δm and M_{D^0} . In order to study the influence on the errors of the mixing parameters, the D^0 lifetime dependence of the background is approximated by the same distribution as the signal. Considering the signal to background ratios for WS and RS from Chapter 10 the expected number of background events B_i in every bin can be calculated. From the number of background in every time bin the error ΔN_i^* on the number of signal events N_i is estimated by:

$$\Delta N_i^* = \sqrt{(\Delta N_i)^2 + (\Delta B_i)^2} \quad (11.3)$$

This estimation is done for WS and RS events and the error on $R(t) = N_{WS}/N_{RS}$ can be calculated by error propagation. The resulting distribution for $R(t)$ is shown in Figure 11.5. The inner error bars of the data points are the statistical error of the signal only and the outer ones includes the contribution from the background. The errors of the mixing parameters are summarized in Table 11.2. The errors are quite large. Systematic errors are not studied yet.

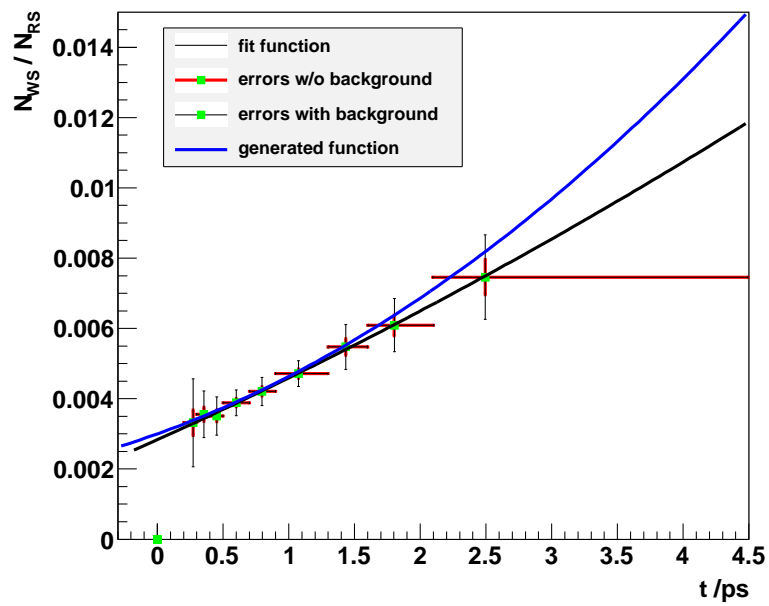


Figure 11.5: Ratio $R(\Delta t_i) = \#WS/\#RS$. The inner errors are the statistical errors of the signal only. The outer error bars include the contribution from the background.

Chapter 12

Summary and Conclusion

In this thesis a Monte Carlo based simulation study towards a $D^0 - \bar{D}^0$ mixing measurement using the decay $D^0 \rightarrow K\pi$ at the LHCb detector is presented. In order to determine the flavour of the D^0 at production time D^0 from $D^* \rightarrow D^0\pi_S$ decays are chosen and the D^* 's in turn are required to originate from the primary vertex. The method for the extraction of the mixing parameters described in this work uses the number of WS (N_{WS}) and RS (N_{RS}) decays per D^0 lifetime bin Δt_i . The mixing parameters can be determined by a binned fit of the ratio $R(\Delta t_i) = N_{WS}(\Delta t_i)/N_{RS}(\Delta t_i)$.

Candidates are selected based on momentum, vertex and track quality, pointing variables and on particle identification. Especially, the particle identification is an important selection criterion.

The remaining background after the selection was discussed and the level of background determined, where possible. An important type of background are D^* 's originating from a secondary vertex. A method to separate those D^* 's from the signal still needs to be developed. Using the minimum bias Monte Carlo sample the expected signal yield was calculated. 1.8×10^6 RS events are expected in an integrated luminosity of $100pb^{-1}$. This corresponds to approximately one week of acquiring data at nominal conditions. The background was estimated by a two dimensional unbinned maximum likelihood fit to the $\Delta m - M_{D^0}$ distribution of selected events. The fit provides an estimate for the ratio of signal to background events of $S/B \approx 0.19$ for WS candidates and $S/B \approx 54$ for RS candidates.

The signal is triggered mainly by the hadron lines of the Level 0 trigger (L0) and the first stage of the high level trigger (HLT1). For the L0 trigger a trigger

efficiency of $(64.8 \pm 0.16)\%$ and for the HLT1 an efficiency of $(47.91 \pm 0.02)\%$ was found.

The effective lifetime resolution of the D^0 was measured to be approximately 47ps. Here, the primary vertex was used as production vertex because of the short lifetime of the D^* .

In a simplified Monte Carlo experiment the effect of the D^0 lifetime acceptance caused by trigger and selection on the errors of the mixing parameters was studied and it was shown that the effect is small. With the results of the 2-dim fit procedure the background contribution to the errors of the mixing parameters was estimated. It shows that the level of background in the WS signal is critical for the analysis.

With the expected yield of reconstructed $D^0 \rightarrow K^\pm \pi^\mp$ decays (1.8×10^6 RS and 6250 WS events @ $100pb^{-1}$) from prompt D^* 's LHCb will be able to improve the measurement of the mixing parameters.

Bibliography

- [1] B. Aubert et al. for the BABAR Collaboration. Evidence for D^0 -anti- D^0 Mixing. *Physical Review Letters*, 98:211802, 2007.
- [2] CDF Collaboration: T. Aaltonen. Evidence for D^0 - D^0 bar mixing using the CDF II Detector. *Physical Review Letters*, 100:121802, 2008.
- [3] C. Amseler et al.(Particle Data Group). D^0 - D^0 bar mixing (Rev.). *Physics Letters B* 667,1, 2008.
- [4] Joerg Marks for the BABAR Collaboration. D^0 - D^0 bar Mixing: An Overview, 2008.
- [5] Fernando Martinez Vidal on behalf of the BaBar Collaboration. Review on D^0 -anti D^0 mixing, 2009.
- [6] Adam F. Falk, Yuval Grossman, Zoltan Ligeti, and Alexey A. Petrov. $SU(3)$ breaking and $D - D$ mixing. *Phys. Rev. D*, 65(5):054034, Feb 2002.
- [7] I. I. Bigi and N. G. Uraltsev. D^0 - oscillations as a probe of quark-hadron duality. *Nuclear Physics B*, 592(1-2):92 – 106, 2001.
- [8] Alexey A. Petrov. Hunting for CP violation with untagged charm decays. *Phys. Rev. D*, 69(11):111901, Jun 2004.
- [9] R Hierck. Optimisation of the LHCb detector. Technical Report LHCb-2003-114, CERN, Geneva, Sep 2003.
- [10] The LHCb collaboration. The LHCb Detector at the LHC. *JINST 3 S08005*, 2008.
- [11] The LHCb collaboration. *LHCb magnet: Technical Design Report*. Technical Design Report LHCb. CERN, Geneva, 1999.

-
- [12] The LHCb collaboration. *LHCb VELO (Vertex Locator): Technical Design Report*. Technical Design Report LHCb. CERN, Geneva, 2001.
- [13] The LHCb collaboration. *LHCb inner tracker: Technical Design Report*. Technical Design Report LHCb. CERN, Geneva, 2002. revised version number 1.
- [14] The LHCb collaboration. *LHCb outer tracker: Technical Design Report*. Technical Design Report LHCb. CERN, Geneva, 2001.
- [15] J Van Tilburg and M Merk. *Track simulation and reconstruction in LHCb*. *oai:cds.cern.ch:885750*. PhD thesis, Vrije Univ. Amsterdam, Amsterdam, 2005. Presented on 01 Sep 2005.
- [16] The LHCb collaboration. *LHCb trigger system: Technical Design Report*. Technical Design Report LHCb. CERN, Geneva, 2003. revised version number 1 submitted on 2003-09-24 12:12:22.
- [17] The LHCb collaboration. *LHCb calorimeters: Technical Design Report*. Technical Design Report LHCb. CERN, Geneva, 2000.
- [18] The LHCb collaboration. *LHCb muon system: Technical Design Report*. Technical Design Report LHCb. CERN, Geneva, 2001.
- [19] The LHCb collaboration. *LHCb RICH: Technical Design Report*. Technical Design Report LHCb. CERN, Geneva, 2000.
- [20] J. Albrecht and U. Uwer. *Fast Track Reconstruction for the High Level Trigger of the LHCb Experiment*. *oai:cds.cern.ch:1211566*. PhD thesis.
- [21] The CLEO Collaboration: J. L. Rosner. Determination of the Strong Phase in $D^0 \rightarrow K^+\pi^-$ Using Quantum-Correlated Measurements. *Physical Review Letters*, 100:221801, 2008.
- [22] Belle Collaboration: M. Staric. Evidence for $D^0 - \bar{D}^0$ Mixing. *Physical Review Letters*, 98:211803, 2007.
- [23] A. J. Schwartz. D^0 - D^0 bar Mixing and CP Violation: HFAG Combination of Parameters, 2009.

-
- [24] I. Belyaev et al. Simulation application for the LHCb experiment. *physics/0306035*, 2003.
- [25] T. Sjöstrand et al. Pythia. *Computer Physics Commun.*135 238, 2001.
- [26] GEANT4 collaboration. *Nucl. Inst. and Methods A* 506,250, 2003.
- [27] Boole. LHCb simulation software.
- [28] C. Amsler et al. (Particle Data Group). *Physics Letters B*667, 1, 2008.
- [29] Mat Charles; Patrick Spradlin; Guy Wilkinson; Philip Xing. Charm mixing: y_{CP} with a tagged $D^0 \rightarrow HH$ sample and a lifetime-binned fit. Presentation at 54th LHCb week (02.12.2009).
- [30] Funai Xing Patrick Spradlin, Guy Wilkinson. A study of tagged $D^0 \rightarrow hh'$ decays for D^0 - D^0 bar mixing measurements. LHCb-2007-049.
- [31] Rene Brun and Fons Rademakers. ROOT - An Object Oriented Data Analysis Framework. Technical report, Nucl. Inst. & Meth. in Phys. Res. A 389 (1997) 81-86. See also <http://root.cern.ch/>.
- [32] David Kirkby Wouter Verkerke. The RooFit toolkit for data modeling. Technical report, arXiv:physics/0306116v1, 2003.
- [33] J Marks and P Weidenkaff.

Erklärung

Ich versichere, dass ich diese Arbeit selbständig verfasst und keine anderen als die angegebenen Quellen und Hilfsmittel benutzt habe.

Heidelberg, den 15. Februar 2010
